

CARDIAC SINGLE PHOTON EMISSION COMPUTED TOMOGRAPHY (SPECT) SIMULATION USING
THE XCAT PHANTOM AND THE SIMIND PACKAGE

by

ADEBAYO T. AKOLADE

THESIS

Submitted in partial fulfillments of the requirements for the degree of
Master's of Science in Physics at
the University of Texas at Arlington
August 2022

Arlington, Texas

Supervising Committee:

Dr Jin Mingwu, Supervising Professor

Dr Qiming Zhang

Dr Yujie Chi

Copyright by
Adebayo T. Akolade
2022

Acknowledgements

I thank Dr Jin, my supervising Professor, for his help in getting me acquainted with the programming skills and medical knowledge required for this project. I would also like to thank Zhou Shiwei, my research colleague, for exposing me to the relevant research materials needed to commence the simulations.

List of Illustrations

Illustration	Page
1. Myocardial perfusion imaging procedure.....	3
2. Components of an Anger camera.....	4
3. Projection Image of a male phantom showing high liver uptake of a technetium-99m radiopharmaceutical.....	5
4. Imaging degradation in SPECT.....	7
5. Effect of attenuation correction on reconstructed images.....	8
6. The four steps in a SPECT simulation study.....	9
7. A Bezier patch	11
8. Activity map of a Male phantom.....	24
9. Attenuation map of a Male phantom.....	15-16
10. Activity map depicting the Left Ventricle of a female phantom	16
11. Attenuation map depicting the Left Ventricle of a female phantom	17
12. Oblique definition through a 3D heart	18
13. Defect Present Phantom of a Male patient.....	20
14. Lesion at the mid inferoseptal on a male patient.....	21
15. Ischemic severity on the anterior wall of a male patient's lv.....	22
16. Lesion at the anteroseptal region on a male subject.....	23
17. Male patient with ischemic severity in the anteroseptal wall.....	23
18. Ischemic severity on the anterolateral wall of a male patient's lv.....	24
19. Standard oblique view of a dpp at anterolateral wall of the lv.....	24
20. Ischemic severity on the inferolateral wall of a male patient's lv.....	25
21. Standard oblique view of a dpp at inferolateral wall of the lv.....	25
22. Lesion at the inferoseptal wall of the lv on a male patient.....	26
23. CSImport validation of severity located at the inferoseptal wall of the lv.....	26
24. ^{99m} Tc energy spectra.....	31
25. PMT Arrays.....	32
26. LEGP-simulated point source in a cylindrical phantom.....	32
27. Energy Spectra of a Tc-99m scan of a point source.....	33
28. Coldspot simulation.....	33
29. Projection Image of a male phantom.....	34
30. Complete projections of a male phantom.....	35
31. Projections of a female phantom.....	36
32. Complete projections of a female phantom.....	37

List of Tables

Table	Page
1. Activity ratio for male and female patient.....	15
2. Defect location on a male XCAT Phantom.....	19

ABSTRACT

CARDIAC SINGLE PHOTON EMISSION COMPUTED TOMOGRAPHY (SPECT) SIMULATION USING XCAT PHANTOM AND THE SIMIND PACKAGE

Adebayo T. Akolade, MS

The University of Texas at Arlington, 2022

Supervising Professor: Dr Jin Mingwu

Clinical data indicates a prevalence of transmural perfusion defects in the apical, mid, and basal segment of the left ventricle (LV) wall in patients with coronary artery diseases (CAD). To administer therapeutic regimes on myocardial function, detection of lesions in various region of the LV wall is essential. Cardiac single photon emission computed tomography (SPECT) is one of the most prevalent diagnostic tools to detect perfusion defects. Computer simulation using digital phantoms based on real patient data obtained from National Library of Medicine (NLM) offers a cost-effective approach to generate realistic imaging data to test novel imaging hardware and software ideas in the first place. This work aims to simulate cardiac SPECT using the Monte Carlo simulation (MCS) of 4D extended cardiac-torso (XCAT) Phantoms. In the first part of this work, we used the XCAT phantom program to generate different patients and perfusion defects at different location and with different sizes and severity. The XCAT phantoms are generated using nonuniform rational B-spline (NURBS) and subdivision surfaces to fit the real patient computed tomography (CT) data to provide detailed anatomical structures, as well as flexibility of definition of patient physiological motion and perfusion defects. The generation of a population of patients will provide a database that is important to investigate the impact of advanced SPECT reconstruction and compensation strategies for different patients and perfusion defects. In the second part of this work, we used the MCS package – SIMIND – to mimic ^{99m}Tc -sestamibi SPECT perfusion imaging of the XCAT phantom. The radiotracer decay, gamma photon transportation inside the human body, and photon detection by the gamma

camera can be simulated in SIMIND accurately. The projection data from SIMIND highly resembles the real data acquired by a real SPECT system. These data will be used to develop and evaluate the compensation strategies for dual cardiac-respiratory gated SPECT for cardiac perfusion imaging to significantly improve the benefit-and-risk ratio of this prevalent diagnostic tool.

TABLE OF CONTENTS

ACKNOWLEDGEMENTS.....	
LIST OF ILLUSTRATIONS.....	
LIST OF TABLES.....	
ABSTRACT.....	
CHAPTER ONE: Overall view of Single Photon Emission Computed Tomography (SPECT) and Cardiac Perfusion Imaging.....	1
CHAPTER TWO: The Extended Cardiac-Torso (XCAT) Phantoms	10
CHAPTER THREE: Monte Carlo Simulation of cardiac SPECT.....	28
CHAPTER Four: Conclusion and Future Work.....	38
APPENDIX	
1. XCAT.....	39
2. CSImport.....	40
3. Simind Program.....	41-42
LITERATURE CITED.....	43-44

CHAPTER 1

Overall view of Single Photon Emission Computed Tomography (SPECT) and Cardiac Perfusion

Imaging

Emission Tomography (ET) is a functional imaging tool that examines diseases by forming a 3D radiotracer distribution inside the human body. The radiotracer injected to the patient body, also called radiopharmaceutical, is composed of a drug that can bond to a particular chemical or molecular process of the targeting organs and a radioisotope that serves as an imaging reporter to emit signals detectable outside the patient body. ET combines the tracer principle with tomography to produce 3D functional images in contrast to X-ray computed tomography (CT) for anatomical structures¹. There are two major modalities for ET based on the radioisotope used as the imaging reporter: 1) Single Photon Emission Computed Tomography (SPECT) using a single-photon emitter i.e., each nuclear decay generates a single gamma photon; 2) Positron Emission Tomography (PET) using a positron emitter where the positron from nuclear decay will annihilate a nearby electron to emit a pair of 511 KeV photons in opposite directions. For SPECT, the gamma camera made of collimator, scintillator, photomultiplier, etc. is used to collect the photons emitted from the patient body from multiple angles. Then tomographic image reconstruction can be used to obtain the 3D distribution of the radiotracer.

A typical cardiac SPECT perfusion imaging is shown in Fig. 1. A SPECT study is initiated with the administration of a radiopharmaceutical which is absorbed by the targeting organs. For safety reasons, the standard dose of the administered radiopharmaceutical is $\sim 10^4$ counts/s/ml¹, making the data acquisition time about 15-20 mins, much longer than a modern CT scan which is completed in a couple of seconds. Next, a gamma camera with a (parallel hole) collimator is used to detect the gamma rays emitted by the radiopharmaceutical. To generate images of clinical relevance, the ideal radiopharmaceutical for myocardial perfusion imaging (MPI) must have a high myocardial uptake with minimal myocardial distribution; a high target-to-background ratio with low uptake in the gut, lungs, liver, and stomach during data acquisition process; rapid blood clearance; and a linear relationship between myocardial uptake

and coronary blood flow. Of the clinically viable blood-flow markers, the cationic and lipophilic Technetium-99m radiopharmaceuticals such as ^{99m}Tc -sestamibi and ^{99m}Tc -tetrofosmin have proved useful in providing satisfying images for the diagnosis of ischemic heart diseases.⁴ ^{99m}Tc -sestamibi is a common radiopharmaceutical used for cardiac SPECT perfusion imaging. Sestamibi is a drug that can highly concentrate in the normal heart muscle (“myocardium”). If the blood supply to a certain part of myocardium is insufficient due to any blockage or constriction as seen in patients with coronary heart diseases, the concentration of sestamibi at that part will be lower than the rest of myocardium. Since sestamibi is bonded with ^{99m}Tc , which can emit 140 KeV gamma photons, the sestamibi distribution inside the heart can be inferred from the tomographic reconstruction of radioactivity from ^{99m}Tc . Tracer concentration for ^{99m}Tc -sestamibi is maximum \sim 1-minute post-injection, and it depletes to $<5\%$ blood activity 5 minutes post-injection. In a typical stress study, ^{99m}Tc -sestamibi occurs at a dosage of 925MBq (25mCi).^{1,4} With advanced 4D reconstruction, this dosage can be reduced to $1/4^{\text{th}}$ without compromising the diagnostic accuracy.² MPI therefore represent a clinical application of SPECT imaging used to evaluate the functions of the myocardium in patient with intermediate or high likelihood of coronary heart diseases.³ If an MPI test shows a lack of blood flow during exercise or pharmacologically-induced stress, but a normal rest test, it could indicate a narrowed artery, also known as angina. This is the case with patients diagnosed with ischemia where the regional blood flow is noticeably reduced during stress test leading to low absorption of the gamma emitter used for the study. If both stress and rest tests show a lack of blood flow to the heart muscles, it could indicate the regions of the heart muscles have been permanently damaged from a previous oxygen deprivation due to myocardial infarction. Thus, the measurement of regional blood flow proves significant in identifying ischemia, the viability of the myocardium, spatial extent and severity of disease, and the determination of medical intervention.⁴

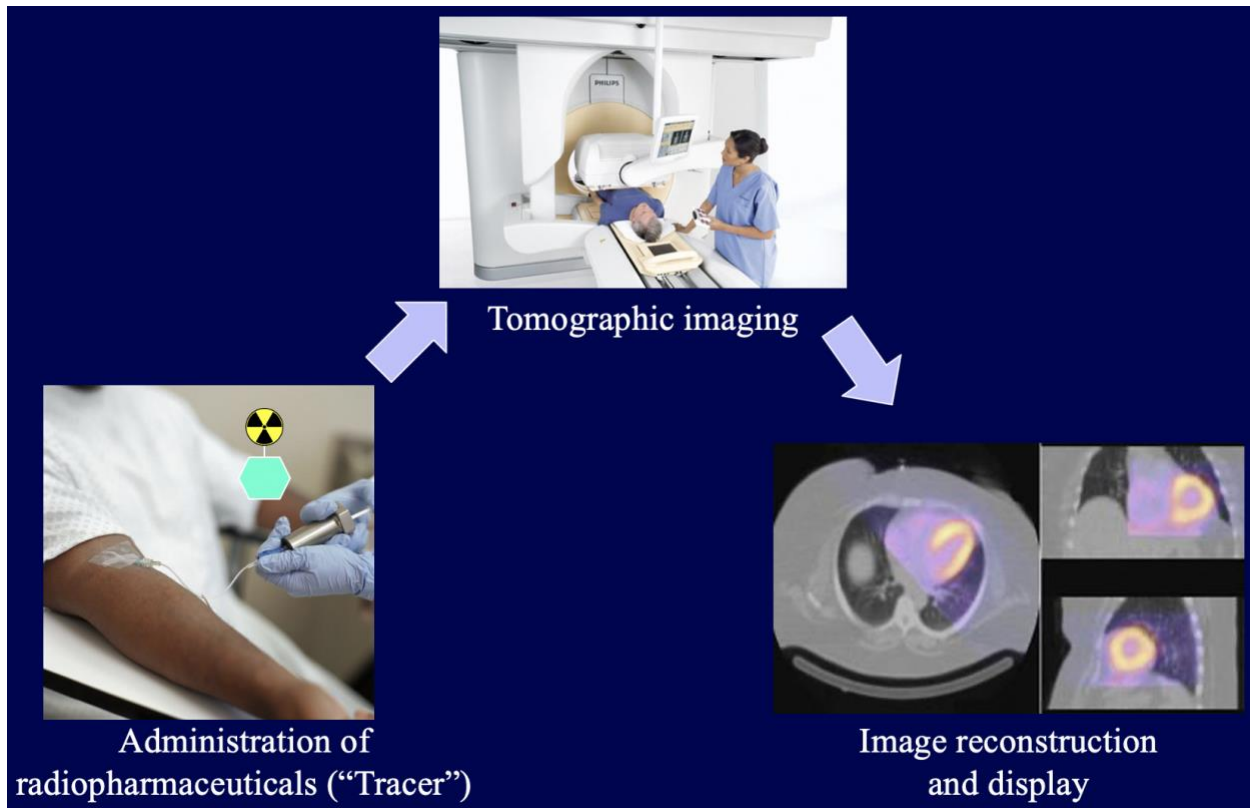


Figure 1. A typical SPECT cardiac perfusion imaging process including three steps: 1) administration of radiotracer; 2) tomographic imaging using the rotating gamma camera around the patient; and 3) image reconstruction and display (the functional image).

A conventional gamma camera is shown in Fig. 2. It is made of collimator, scintillator, light-guide, photomultiplier tubes (PMTs) and the readout electronics which discriminate the photon energies and resolve the location of detected event. The gamma camera will collect 2D planar images of 3D radiotracer distributions of the patient (“image”), so called “projection”. One example of a projection of a XCAT phantom with ^{99m}Tc -sestamibi is shown in Fig. 3, where the liver on the upper left of the image has a high uptake and the heart at the upper right is seen with a lower activity due to the thin heart wall. Part of the kidney is shown on the lower right of the figure. The intense activity observed in the liver is due to the high liver absorption feature characteristic of ^{99m}Tc -sestamibi. Upon absorption, the visualization of the gut and stomach, through radioactive bile, makes it difficult to assess cardiac activity in the left and lower ventricular walls.⁴ As the projections are the Radon transform of the image, the analytic image reconstruction methods, such as filtered backprojection (FBP), or the iterative reconstruction

methods can be used to solve the inverse problem from the projections to the image. The reconstructed functional image can be viewed by the physician for disease diagnosis (sometimes overlaid on the anatomical CT image). Since some parameters such as ventricular ejection fraction, which measure cardiac function, are difficult to visually inspect, the diagnostic decision process can be enhanced for clinical purposes using computer-aided tools. More advanced methods utilize kinetic modelling to describe the time-evolution of the radiotracer distribution, calibrating for blood flow, receptor concentration and other parameters vital to a dynamic study.¹

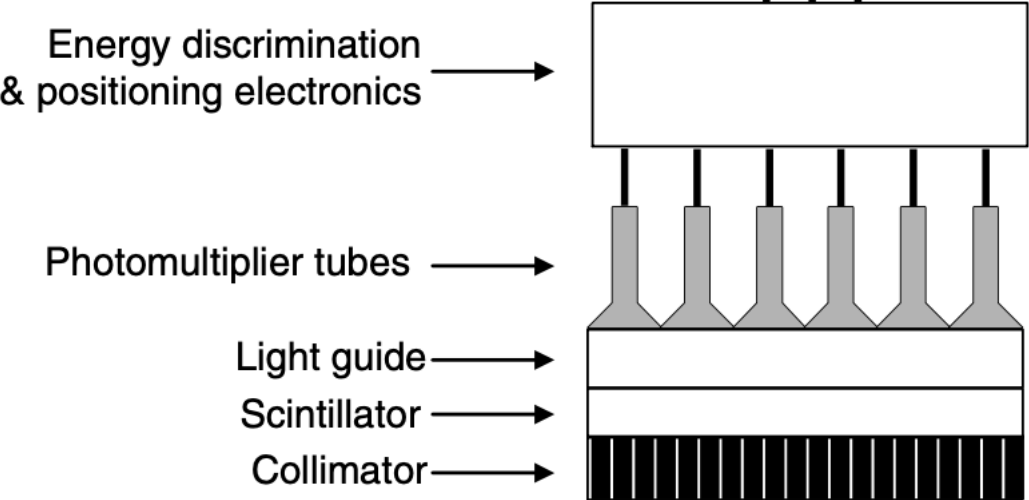


Figure 2. Fundamental components of a gamma camera for 2D projection of 3D image¹.

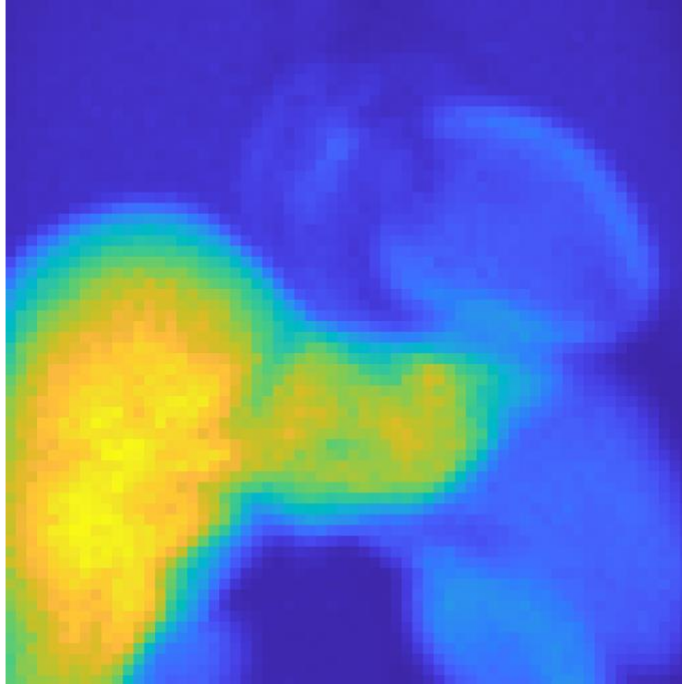
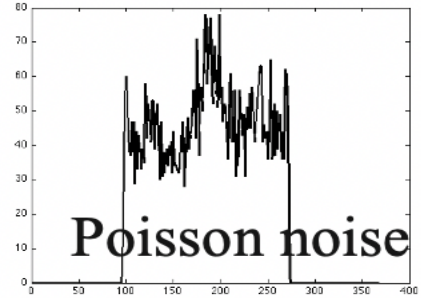
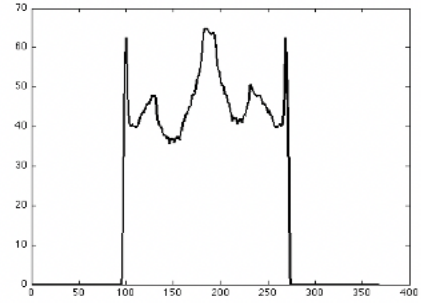
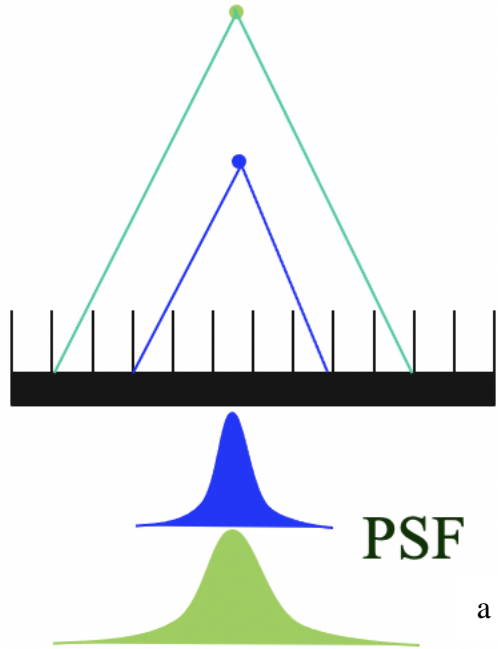


Figure 3. 2D projection of a male XCAT phantom. Projections at different angles around the phantom/patient can be used to reconstruct the 3D image of tracer distribution.

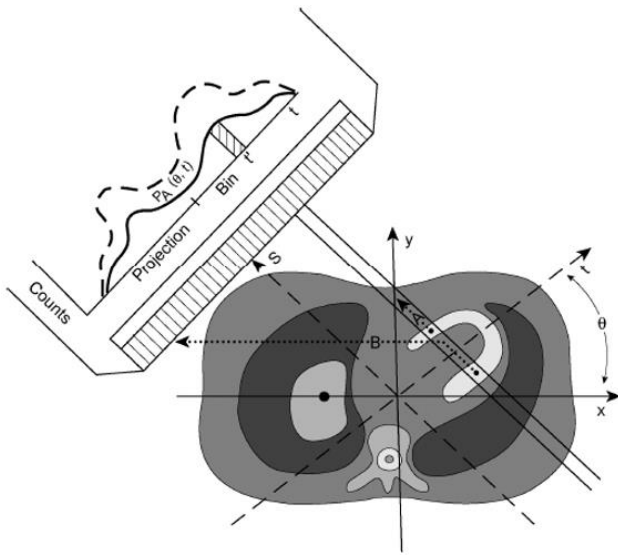
There are four major factors for the degradation of SPECT imaging: distance dependent resolution, low sensitivity (Poisson noise), attenuation, and scatter, as shown in Fig. 4. The distance dependent resolution is caused by the source distance from the parallel hole collimator. The point spread function (PSF) will be wider for the source farther away from the collimator (Fig. 4a). This dispersion of photon over increasing distance contaminates the projection (Fig. 4b upper) with Poisson noise (Fig. 4b bottom) during data acquisition. Due to the collimator, the sensitivity of the gamma camera (# of detected photons/# of all emitted photons) is low. Combined with the amount of radiotracer used in SPECT imaging ($\sim 1.11\text{GBq}$ for imaging with a 140 keV photon with a LEHR collimator), the projections could be very noisy, especially for cardiac or dual cardiac-respiratory gated data acquisition. The attenuation occurs when the photon never reaches the detector due to absorption by a non-uniform attenuator or deflected by the tissue as shown in Fig. 4c. The scatter occurs when the photon is deflected once or multiple times in the patient or collimator before it reaches a detector element, thus recording a wrong event location (Fig. 4d). Inability to resolve the initial location of the scattered photons causes distortion in the resulting image, since each pixel in a tomographic

image serves as an histogram for the spatial location of detected photons. Fig. 5 shows the effect of these degradation factors on the reconstructed images when FBP was used. FBP can perfectly reconstruct the source/activity map if none of degradation factors were modeled in the simulated projection data. However, in real scenario, these factors must be counted in and can be compensated in the reconstruction algorithms. At the absence of scatter, attenuation, and variations in detector efficiency, the number of photons detected is proportional to the tracer concentration contained in the scanned volume of response (VOR): $\iiint s(\mathbf{x})f(\mathbf{x})d\mathbf{x}$, where $s(\mathbf{x})$ represents the sensitivity and $f(\mathbf{x})$ represents the radiotracer distribution.¹ With this, the inverse problem FBP solves can be understood as obtaining $f(\mathbf{x})$ given a set of noisy measurements for all VOR. Both distance-dependent resolution and attenuation can be modeled in VOR and scatter can be estimated and added as an additive term. Post-reconstruction smoothing for FBP or smoothing regularization terms for iterative reconstruction can be used to address the image noise.

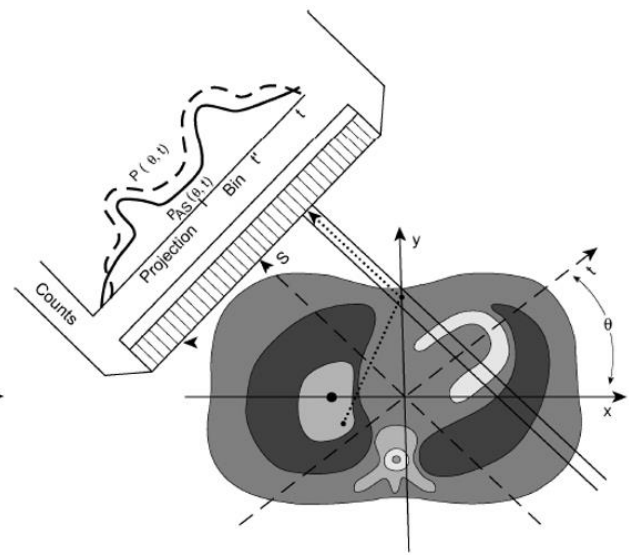


a

b



Attenuation c



Scatter d

Figure 4. Degradation factors for SPECT imaging: a) distance dependent resolution (PSF: point spread function); b) low sensitivity (Poisson noise); c) attenuation; and d) scatter.

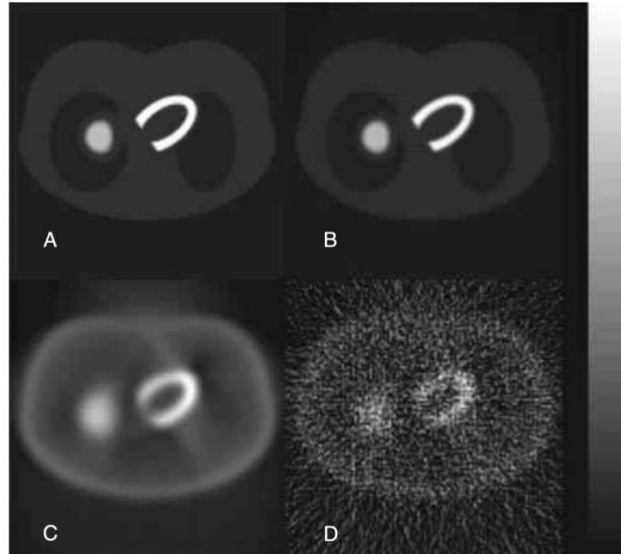


Figure 5. A: Original source distribution; B: FBP reconstruction without attenuation, scatter, spatial resolution, and noise in the projection data; C: FBP reconstruction with attenuation, scatter, and spatial resolution, but without noise in the projection data; D: FBP reconstruction with attenuation, scatter, spatial resolution, and noise in the projection data¹.

As the nuclear decay of the radiotracer, the scatter and absorption of photons, and detection of photons in SPECT are random, Monte-Carlo simulation (MCS) is a powerful tool for development and evaluation of novel hardware and software ideas. A typical simulation study is shown in Fig. 6, which includes four major steps: (1) Generation of virtual patients with anatomical, pathological, and physiological variability using 4D XCAT⁵ (2) SIMIND Monte Carlo simulation (MCS) of SPECT imaging of simulated virtual patients;⁶ (3) reconstruction for SPECT myocardial perfusion imaging; and (4) Task-based performance assessment. In this work, we focus on the first two steps. The results from this work will provide the data to test the novel reconstruction algorithms to alleviate the adverse effect of SPECT degradation factors.

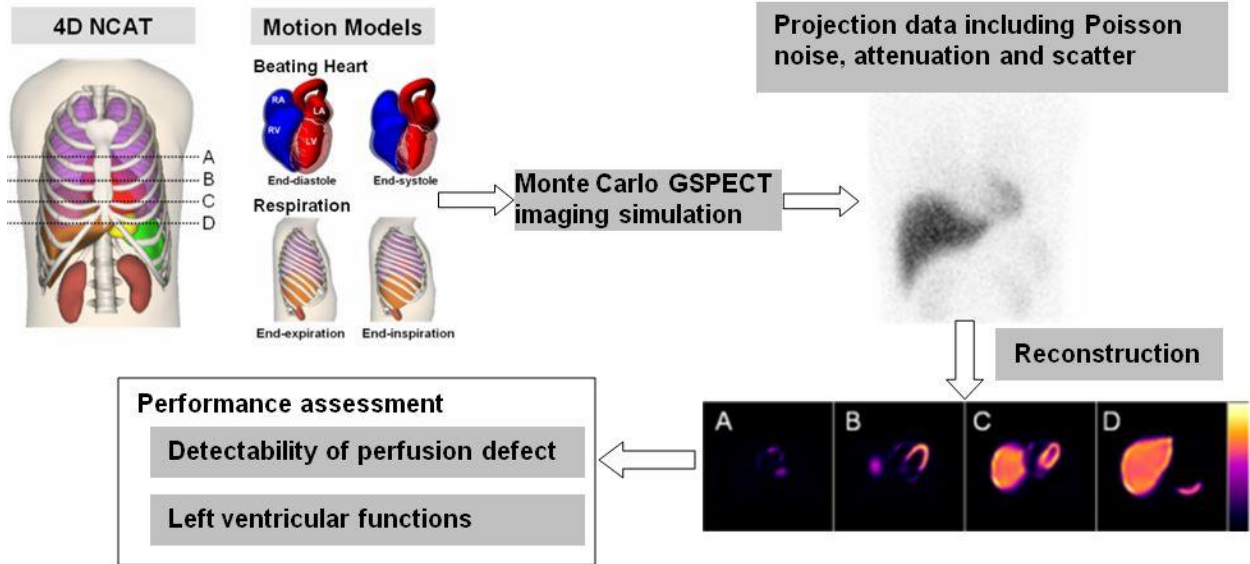


Figure 6. A computer simulation study of cardiac SPECT imaging. Four major steps are: (1) Generation of virtual patients with anatomical, pathological, and physiological variability using 4D XCAT (2) SIMIND Monte Carlo simulation (MCS) of SPECT imaging of simulated virtual patients; (3) reconstruction for SPECT myocardial perfusion imaging; and (4) Task-based performance assessment. In this work, we focus on the first two steps.

CHAPTER 2

The Extended Cardiac-Torso (XCAT) Phantoms

The 4D XCAT phantom⁵ was developed by Dr. Paul Segars at Duke University. The phantom program can generate both the attenuation map (for the patient anatomy of CT images) and the activity map (for the radiotracer distribution of PET images) based on real patient data. The realistic motion models of human respiratory and cardiac motion are also included to enable 4D studies (3D space + 1D time). The phantom's flexibility with the aid of non-uniform rational B-spline (NURBS) surfaces allows the creation of models with user-defined deformities needed for a realistic simulation study. In this chapter, we first introduce the mathematic principles of XCAT phantom. Then we present how to generate different patient activity maps and attenuation maps, for imaging radiotracer distribution, our primary goal, and accruing data necessary for attenuation compensation during reconstruction process. Finally, we demonstrate how to embed the perfusion defects at different locations with various sizes and severities.

2.1 XCAT phantom

Mathematical phantoms have greater flexibility since they are based on geometric primitives that can be simulated at any resolution at the absence of errors that results from interpolation. Non-Uniform Rational B-Splines (NURBS) are mathematical representations of 3D geometry that can accurately construct standard 2D geometric objects like lines, circles, ellipses, tori, and design free-form 3D objects such as the XCAT-generated phantoms of the human body.⁹

Degrees, control-points, knots and evaluation rule define a NURBS curve. The NURBS shapes are user-defined and manipulated by toggling with the degrees which can assume four integer values 1, 2, 3, 4 corresponding to linear, quadratic, cubic and quintic respectively. To alter a geometric shape with NURBS, we define the quantity degree+1 as the order of the NURBS curve. In this form, the control points are a collection of all order points so that reducing the degree of a NURBS curve changes its control points which consequently

changes its shape. It is noted that increasing degree doesn't necessarily change its shape. Control points defining a Bezier patch are shown in figure 7.

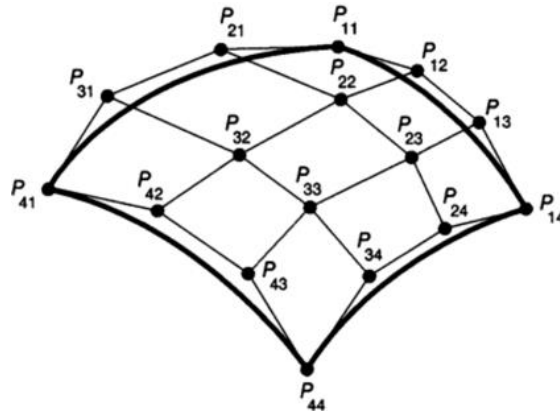


Figure 7. Control points on a Bezier surface converted from a $n \times m$ NURBS surface.

The NURBS surfaces are non-rational when the weights associated with the control points are of equal value– 1 for lines and polylines. In rational form, the NURBS curve is represented by^{9,10}

$$R(t) = \frac{\sum_{i=1}^n w_i \mathbf{p}_i N_{i,k}(t)}{\sum_{i=1}^n w_i N_{i,k}(t)}, \quad (1)$$

where n is the number of control points \mathbf{p}_i , w_i is the weight associated with the control points, and N_i is the B-spline basis function. If $w_i=1$, the integral B-spline surface is recovered. The evaluation formula receives input parameters and produces a point location. The geometry of the NURBS is used to form voxelized phantoms with organ shapes limited by the modeling equations. Voxels which constitute the phantoms are segmented by colors and identifiers on each voxel organs. With a fixed image resolution, transforms can be applied to these phantoms to simulate variations in body anatomy and patient motion in a computerized phantom which requires interpolation. Since the method produces digital images at a specified location and resolution, ray tracing technique used in transmission tomography studies are not applicable.

The XCAT voxelized phantoms used for SIMIND simulation was constructed by NURBS surfaces of $n \times m$ control points converted into $n \times m$ cubic Bezier patches so that patch forming a convex-hull shape of 16 control points approximating the shape of the surface. Bezier surfaces are approximated by inserting multiple knots into the NURBS surface with multiplicity of 4. This addition helps determine the uniformity of knots on the NURBS surfaces. Equally spaced Knots starting with a full multiplicity– knot value duplicated limited by the degree value,

i.e., 5 for organic free-form shapes—, followed by a simple knot, then terminated with a full multiplicity knot are called uniform. For example, a uniform knot of degree 3 with 7 control points could be 1,1,1,2,3,4,5,5,5. Interchanging the sixth number in the list with a 7 would lead to non-uniform shapes as controlled by the Knots. Duplicate knot values at the middle of the list creates either a smooth curve or a NURBS curve with a sharp bent given the duplicate are of full multiplicity. A NURBS surface patch can be represented by^{9,11}:

$$r(u,v) = \frac{\sum_{i=1}^m \sum_{j=1}^n w_{i,j} \mathbf{p}_{i,j} N_{i,k}(u) N_{j,l}(v)}{\sum_{i=1}^m \sum_{j=1}^n w_{i,j} N_{i,k}(u) N_{j,l}(v)} \quad (2)$$

where $\mathbf{p}_{i,j}$ are the control points, $w_{i,j}$ represents the weighting factors, and $N_{i,k}(u)$ and $N_{j,l}(v)$ represent the two B-Spline basis functions that generate the NURBS surface. In all cases, i and j in Eqn. 2 represent the control points, and k and l correspond to the degree of the basis function.

With $w_{i,j} > 0$, this expression can represent quadrics, ellipses, tori and free-form surfaces like car bodies and human bodies. When the number of control points equal the order of the B-Spline function in both u and v coordinate of the b-spline basis functions, the NURBS surface reduces to rational Bezier surface patch¹¹:

$$R(u,v) = \frac{\sum_{i=0}^m \sum_{j=0}^n w_{i,j} \mathbf{b}_{i,j} B_{i,m}(u) B_{j,n}(v)}{\sum_{i=0}^m \sum_{j=0}^n w_{i,j} B_{i,m}(u) B_{j,n}(v)} \quad (3)$$

Organ shapes are represented with a boundary box restricted within the minimum and maximum values of $r(x,y,z)$ in the matrix of control points is defined with the plane equation:

$$Ax + By + Cz + D = 0, \quad (4)$$

where A, B, C are cross vector coefficients $(A, B, C) = \mathbf{V}_1 \times \mathbf{V}_2$ used to defined the plane. \mathbf{V}_1 and \mathbf{V}_2 are related to the 3 control points – $\mathbf{P}_1(x_1, y_1, z_1)$, $\mathbf{P}_2(x_2, y_2, z_2)$, $\mathbf{P}_3(x_3, y_3, z_3)$ – used to define the plane by: $\mathbf{V}_1 = \mathbf{P}_2 - \mathbf{P}_1$ and $\mathbf{V}_2 = \mathbf{P}_3 - \mathbf{P}_1$. The coefficient D is obtained from rearranging equation 4:

$$D = -A*x_1 - B*y_1 - C*z_1. \quad (5)$$

To improve the projection algorithm, each XCAT organ is defined with a bounding volume hierarchy (BVH), a tree of bounding volumes which encompasses all bounding volumes within it. This method is more efficient because the bounding volume better represents the shapes of the organs such that when a ray misses the bounding volume on a certain node, it skips all the children in its tree, thereby reducing the testing of planes that do not intersect with the ray and increasing computational speed of the projection images. Modern computer graphics techniques also improve the ray-box intersection routine by requiring the BVH treated as a series of slabs with the distance to the nearest and farthest point of the ray computed for each slab. The ray intersects with the box when the largest near value is less than the smallest far value; otherwise, it misses the box. The improved ray-box routine is computationally favorable as it only requires 6 multiplication and 6 subtraction routines as opposed to 90 multiplication/division and 108 addition/subtraction required for ray-surface calculation with six planes.¹¹ The intersection points are vital to construct line segment path through the organs in the XCAT phantom. Note that in SIMIND simulation, if the voxelized phantoms are used, the aforementioned computational treatment will not be utilized.

2.2 Generation of activity maps and attenuation maps of normal patients

In order to generate a XCAT phantom, we need to define a parameter file, called “general.samp.par”. First, we set the variable “MODE” value to “0”. This sets up the program to generate phantoms. To generate a male phantom, we do as follows:

- Set “heart_base” to “vmale50_heart.nrb”
- Set the “gender” variable to “0” for male
- Set the value of “organ_file” to “vmale50.nrb”
- To run the program, type: `dxcat2 general.samp.par SIMULATION_NAME`, where “SIMULATION_NAME” is the name defined by the user to save the file.

The generated 2D slices of 3D phantom begin at the bottom and move upward the body with increasing slice number.

The male phantom (a defect absent phantom (DAP)) is 175.23 cm in height, and has a chest circumference of 99.36 cm. The cardiac slices begin at the torso and end, after 301 slices, at the brain. The short axis of the patient chest is 23.21 cm in extent while the long axis is 32.52

cm. The male patient has a left ventricle chamber volume of 139.79 ml, and the volume of the LV myocardium is 110.44 ml. With the volume of the right ventricle and both atrial volumes, the male phantom has a total heart volume of 909.04 ml. Four transverse slices pertinent to an MPI study of a male patient’s activity maps are shown in Fig. 8. All slices represent an activity map of the radiotracer in the target organs, including the heart (the thicker one is LV).

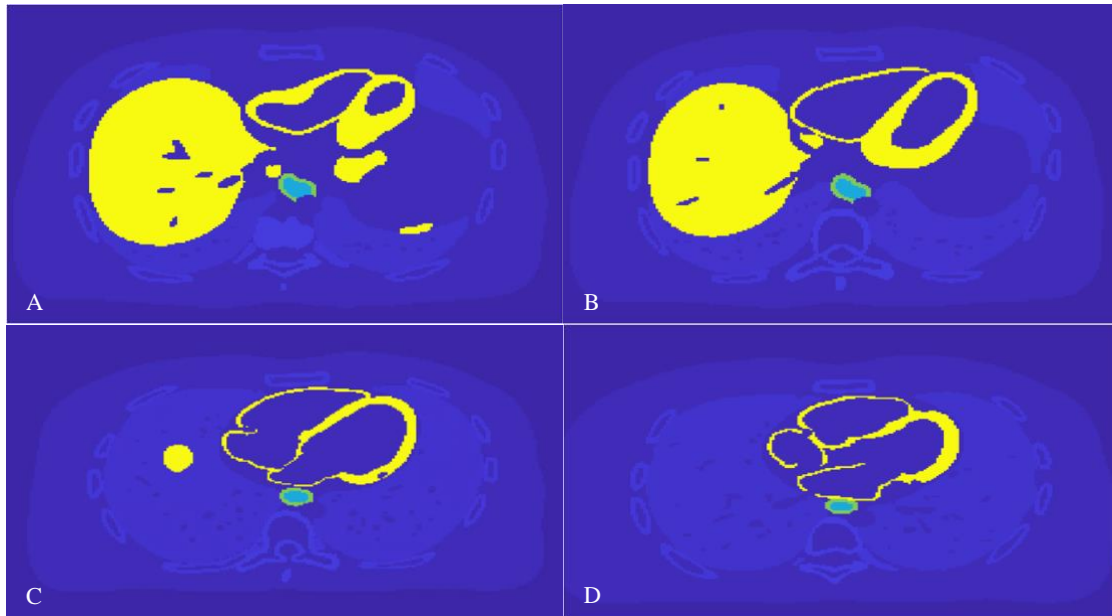


Fig 8. Heart slices of a male phantom. a) slice 165; b) slice 170; c) slice 190; and d) slice 200.

These images provide the radiotracer distribution inside the phantom (“activity map”) for the MC simulation to generate SPECT projection images, e.g. Fig. 3. The activity defined in different organs in XCAT is listed in Table 2.1. For example, for heart we define them in XCAT as follows:

```
myoLV_act = 75.000000
myoRV_act = 75.000000
myoLA_act = 75.000000
myoRA_act = 75.000000.
```

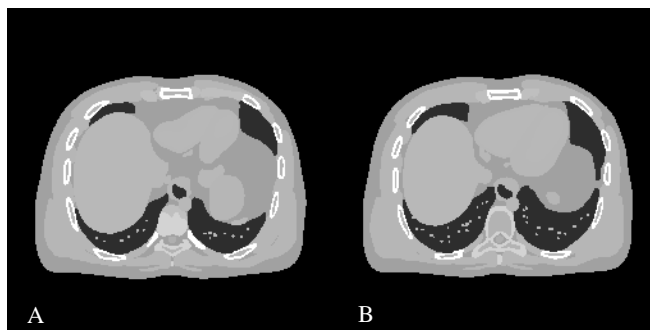
The maximum uptake is 75.00 (yellow in activity maps, e.g. Fig. 8) and a background activity is 2.00. Note that these are not the absolute radioactivity of ^{99m}Tc-sestamibi, but rather the relative concentration. The projection will be scaled to the clinical counts in the following Monte Carlo simulation.

Organ	Activity Ratios
Heart	75

Liver	75
Gall Bladder	60
Left lung	4
Right lung	4
Esophagus contents	30
Esophagus	50
Left kidney cortex	75
Right kidney cortex	75
Left kidney Medulla	75
Right kidney Medulla	75
Body	2

Table 2.1 Radioactivity levels for major organs defined for a male XCAT phantom for ^{99m}Tc -sestamibi.

The corresponding attenuation maps are shown in Fig. 9, which contain important information about gamma photon attenuation and scatter as it propagates through the human body. Both activity maps and attenuation maps are needed for Monte Carlo simulation of SPECT imaging. In reconstruction, simulated attenuation maps can provide ideal transmission tomographic images for attenuation correction, although in real clinic these images are usually collected by X-ray CT.



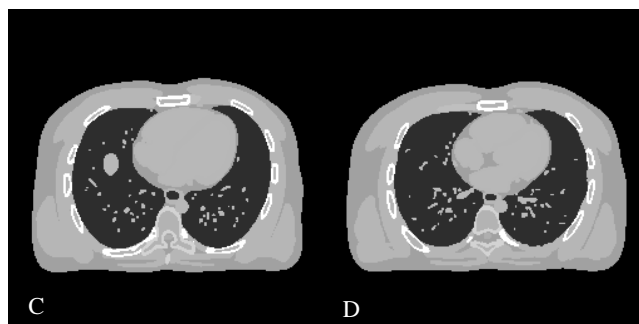


Figure 9. The corresponding attenuation maps of a male XCAT phantom (in Fig. 8). a) slice 165; b) slice 170; c) slice 190; and d) slice 200.

A female phantom of height 163 cm and a chest circumference of 93.99 cm was also simulated from the XCAT program. The short axis view of the patient chest is 21.9 cm in extent while the long axis is 31.4 cm. The female patient has a LV chamber volume of 113.22 ml, and the volume of the LV myocardium is 87.17 ml. With the volume of the right ventricle (RV) and both atrial volumes, the female phantom has a total heart volume of 710.83 ml. The radioactivity of all the major organs of ^{99m}Tc -sestamibi is the same in Table 2.1. Selected cardiac slices of the activity and attenuation maps are shown in Fig. 10 and 11, respectively.

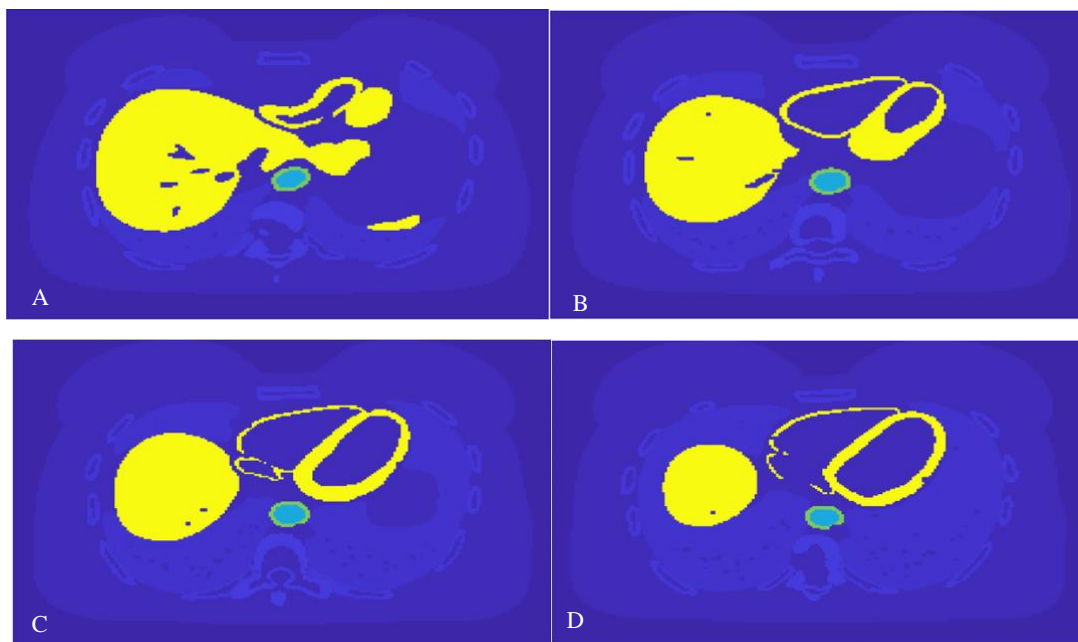


Figure 10 Activity maps depicting the radiotracer concentration on a female phantom. a) slice 95; b) slice 100; c) slice 105; and d) slice 110

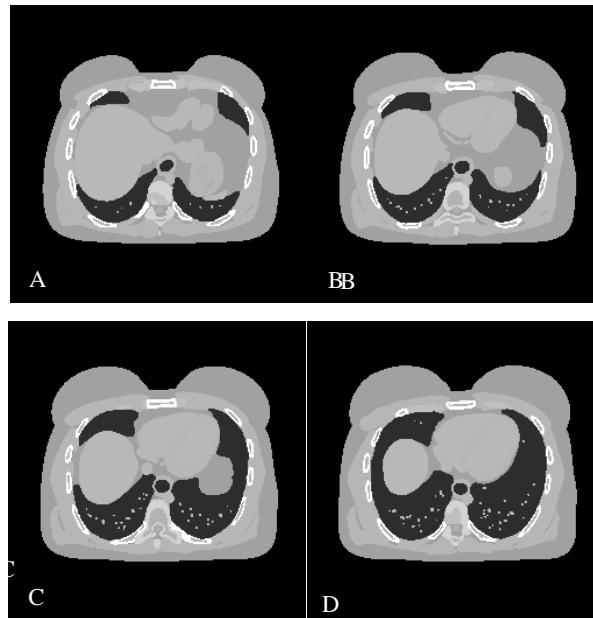


Figure 11. Attenuation maps of a female phantom. a) slice 95; b) slice 100; c) slice 105; and d) slice 110.

Simulated for respiration only, the female patient has a beating heart of 1 seconds and a respiratory period of 5 seconds. At end-diastole, with the female patient fully relaxed, the patient had inhaled 22% within .5000 seconds, and has a diaphragm motion of -3.77 mm.

2.3 Generation of perfusion defects

To make the simulation more realistic, lesions are best simulated at various locations on the left ventricular (LV) myocardium as shown in Table 2.2. Not only are the LV muscles prone to injuries sustained from trauma on the left main coronary artery (LMCA) causing reduced oxygen supply, but also the spatial resolution of SPECT can resolve the thicker LV wall much better than the thinner walls of other heart regions. The cardiac slices used in SPECT, cardiac CT, and PET are displayed and oriented using the standardized nomenclature for cardiac planes¹²: short axis, horizontal long axis and vertical long axis as shown in Fig. 12. The axis are oriented such that the planes transect the apex and center of the mitral valve. For short axis images (from the base to the apex), anterior wall of the LV is on the top and inferior at the bottom, while septal is on the left and lateral on the right. For horizontal long-axis images (from

inferior to anterior), septal is on the left and lateral on the right, while the base of LV is towards the bottom and the apex is on the top. Lastly, for the vertical long-axis images (from septal to lateral), base is on the left and apex on the right, while anterior is on the top and inferior at the bottom. Therefore, in Table 2.2, the last two columns define the axial (from base to apex) and the circumference (septal, lateral, inferior and anterior), respectively. All transmural defects are simulated as 20% and 40% uptake reduction in the LV, with a size of 10% and 20% of the LV volume for each phantom.

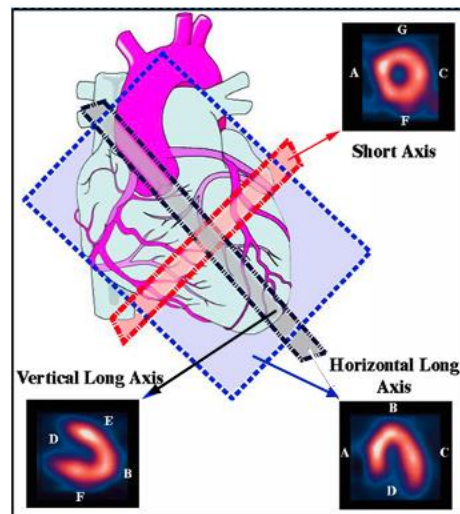


Figure 12. Three orthogonal planes of heart. A: Septal; B: Apex; C: Lateral; D: Base; E(G): Anterior; F: Inferior. (<https://www.people.vcu.edu/~mhcrosthwait/clrs318web/anatomyofthemyocardium.htm>, some errors fixed)

To generate a perfusion defect, we specify the parameters in the XCAT program as follows.

- Change “Mode” to “1.”
- “Gender”, “heart_base” and “organ file” must be set to corresponding sex. For example, if male “gender” were used, male “heart_base” and male “organ file” are needed to generate a correct lesion based on the male organs.
- The variables that affect lesion locations are “ThetaCenter” and “XCenterIndex”. In the first two columns of Table 2.2, we listed all lesions simulated in this work.
- The variables that affect lesion size are “ThetaWidth” and “XWidthIndex.” We adjust them accordingly to obtain lesions with 10% and 20% of LV volumes.
- Run the program: `dxcat2 general.samp.par lesion_name`

Once the perfusion defect was generated, it can be subtracted from the DAP to obtain the Defect Present Phantom (DPP).

ThetaCenter	XCenterIndex	Axial	Circumference
0	1	Apical	Anterior
0	1	Apical	Anterior
180	1	Apical	Anteroseptal (10% of LV vol) Anteroseptal from CSImport
180	1	Apical	Anteroseptal (20% of LV vol) Anteroseptal from CSImport
135	.5	Mid	Anterolateral (10% of LV vol) Anterolateral from CSImport
135	.5	Mid	Anterolateral (20% of LV vol) Anterolateral from CSImport
225	.5	Mid	Inferoseptal (10% of LV vol) Inferoseptal from CSImport
225	.5	Mid	Inferoseptal (20% of LV vol) Inferoseptal from CSImport
45	.1	Basal	Anterior (10% of LV vol) Anterior on CSImport
45	.1	Basal	Anterior (20% lv) Anterior on CSImport
150	.2	Basal	Lateral (10% of LV vol) Lateral from CSImport
150	.2	Basal	Inferolateral (20% of LV vol) Lateral from CSImport

Table 2.2. XCAT parameter settings and the corresponding perfusion defect locations. A clinical program, Cardiac Suite (CSImport), is used to verify the location of lesions specified by the XCAT phantom.

In Fig. 13, a male patient with a lesion of 22.088 ml is shown (brownish orange). The male patient has a left ventricle myocardium volume of 110.44 ml and a total heart volume of 909.04 ml after the first frame, i.e end-diastole and at full exhalation. In the second frame, its

LV myocardium volume remains approximately the same, at 110.34 ml, while the total heart volume increases to 912.44 ml. respiration period of 5 seconds the respiration parameters at 22% inhalation are diaphragm motion of -3.77 ml delta AP diameter of .94 mm. The DPP has a defect at the mid-inferoseptal wall of LV with 20% uptake reduction. A house-developed MATLAB code was used to rotate the DPP to a proper orientation. Then, the rotated DPP was imported in the cardiac suite ("CSImport"), a clinical SPECT image analysis program, to show three cardiac planes of the lesions' location on the LV segment (see Fig. 14). In Fig. 14, the lesion appears as a purple shade. The lesion extends over the middle septal and inferior (and lateral) wall in the short-axis images and the horizontal long axis and appears at the Inferior of the vertical long axis image. This confirms that the lesion location is at the mid-inferoseptal wall. It is noted that the inferior segment in is difficult to assess as extra-cardiac uptake can be caused by sub-diaphragmic liver and gut uptake in the proximity of the heart and infero-apic reduced uptake can be misread as perfusion defect due to abrupt or heavy breathing, soft tissue attenuation caused by large breast or diaphragm, and lastly, apical thinning.¹³ Apical thinning in the anterior segments covered by circumference of the short axis is responsible for the absence of a DPP in that region. Thus, a lesion of 10 or 20 percent the size of the male LV volume could not be achieved.

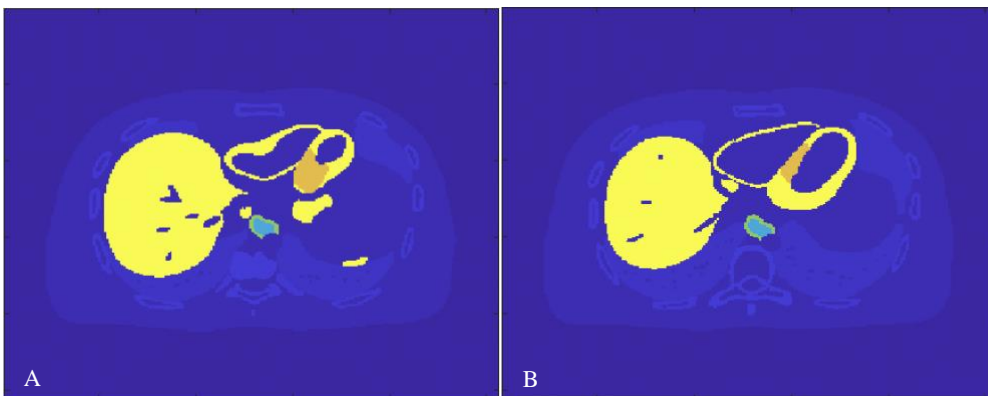


Figure 13. Transverse heart slices of a male Defect Present Phantom (DPP) at mid-inferoseptal wall of LV.

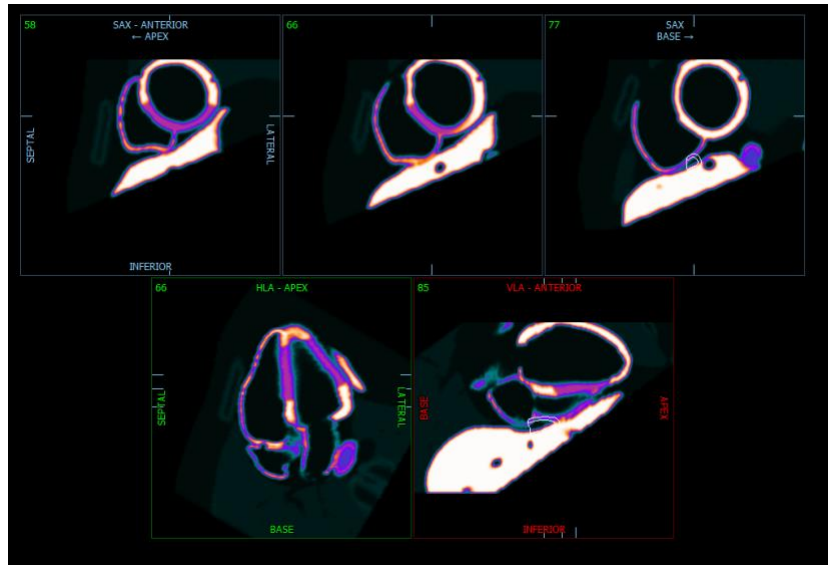


Figure 14. The lesion of Fig. 13 displayed in short-axis, horizontal long-axis and vertical long axis using CSImport.

Several DPPs and their cardiac planes in CSImport are shown as examples in the following figures for anterior, anterolateral, lateral, inferolateral lesions of a male DPP and an inferoseptal lesion of a female DPP. Lesion position parameters vital to generating a lesion are guided by Table 2.2, where “ThetaCenter” and “XCenterIndex” are defined in the XCAT program. The defect in Fig. 15 is in the mid and basal thirds of the LV of the male phantom defined above, representing the region of the LV with reduced blood supply.

Male Anterior Lesion

The transverse slice in Fig. 15a shows a lesion at the base with an uptake reduction of 20% severity (it is small due to the inferior slice). In Fig. 15b, the anterior uptake reduction can be seen in the short axis images (close to the base) and the vertical long axis image.

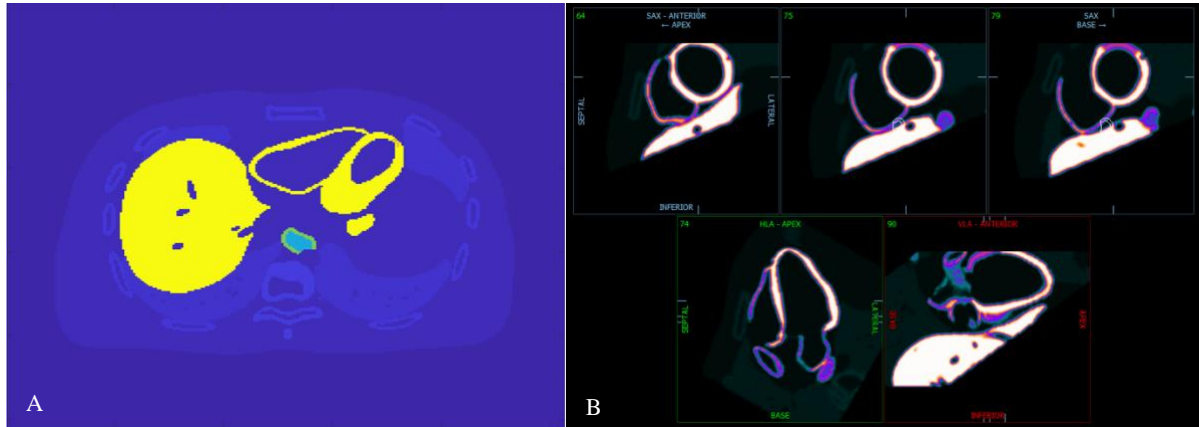


Figure 15. Lesion in the basal anterior wall. A) transverse slice; B) short-axis, horizontal long-axis and vertical long axis images from CSImport

Male Anterolateral Lesion

The transverse slices in Fig. 16 show a lesion at the apex with an uptake reduction of 20% severity. In Fig. 17, the anteroseptal uptake reduction can be seen in the short axis images

(close to the apex) and two long axis images. As the lesion is at the apex, it indeed extends from anterior to inferior and from septal to lateral.

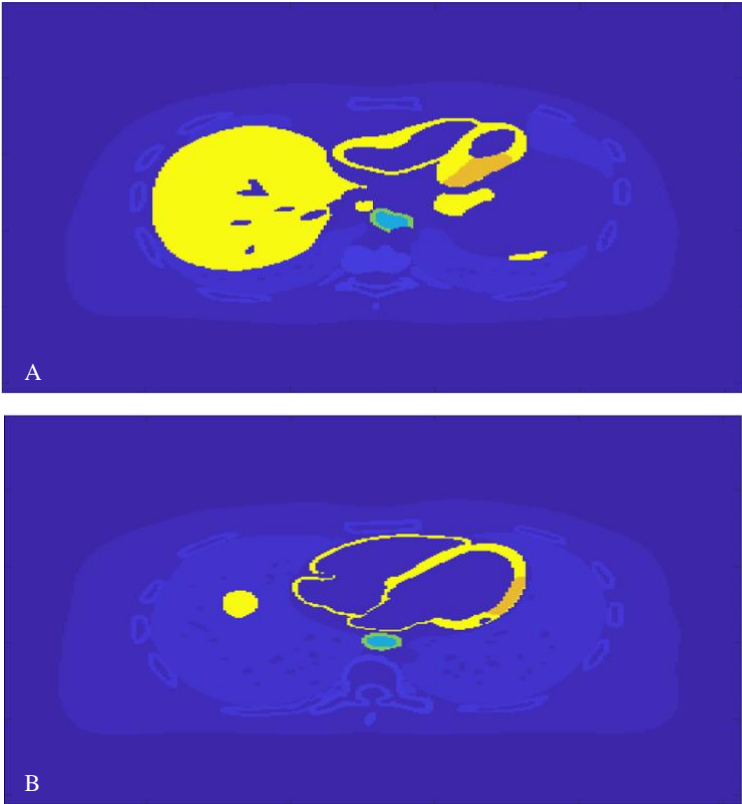


Figure 16. Transverse heart slices of a male Defect Present Phantom (DPP) at anterolateral wall of LV. (a) Slice 165; b) Slice 190

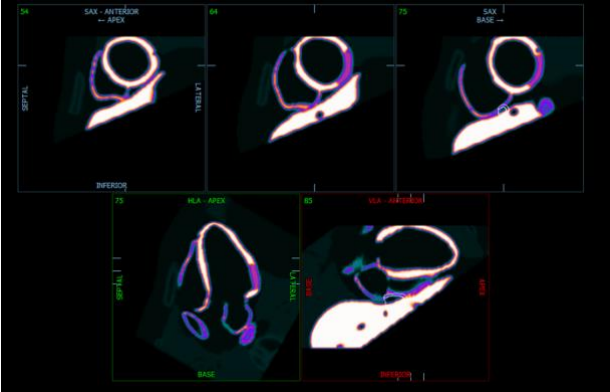


Figure 17. The lesion of Fig. 16 displayed in short-axis, horizontal long-axis and vertical long axis using CSImport.

Male Lateral Lesion

The transverse slices in Fig. 18 show a lesion at the lateral location with an uptake reduction of 20% severity. In Fig. 19, the lateral uptake reduction can be seen in the short axis images (close to the apex) and the horizontal long axis image, but not in the vertical long axis image. Clinically, this corresponds to a lesion due to trauma or a constriction in the left circumflex artery (LCX), the artery assigned to the lateral segments.¹²

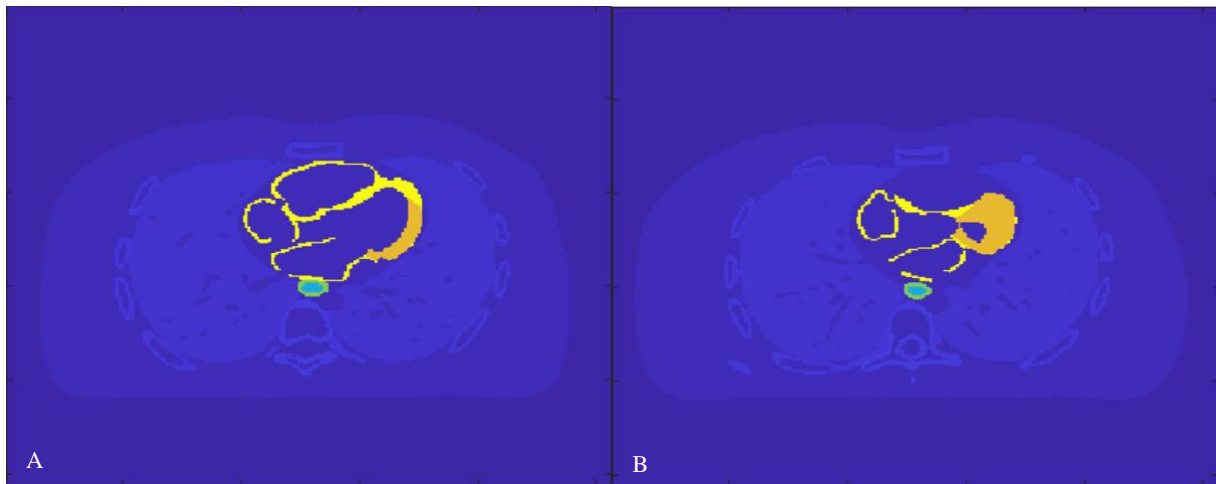


Figure 18. Transverse heart slices of a male Defect Present Phantom (DPP) at lateral wall of LV. (a) Slice 200; 18b) Slice 206)

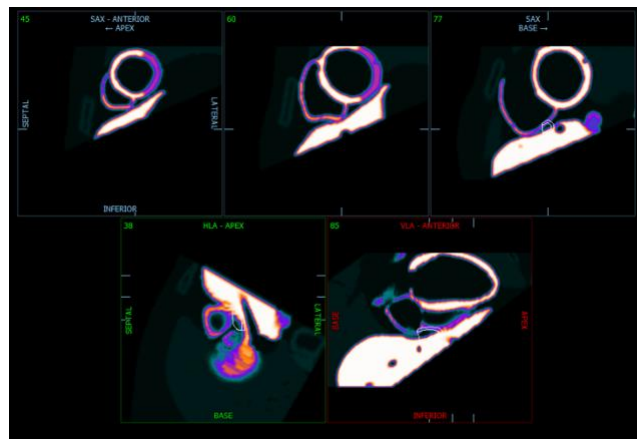


Figure 19. The lesion of Fig. 18 displayed in short-axis, horizontal long-axis and vertical long axis using CSImport.

Male Inferolateral Lesion

The transverse slices in Fig. 20 show a lesion at the inferolateral wall with an uptake reduction of 20% severity. In Fig. 19, the inferolateral uptake reduction can be seen in the short axis images (close to the base) and two long axis images.

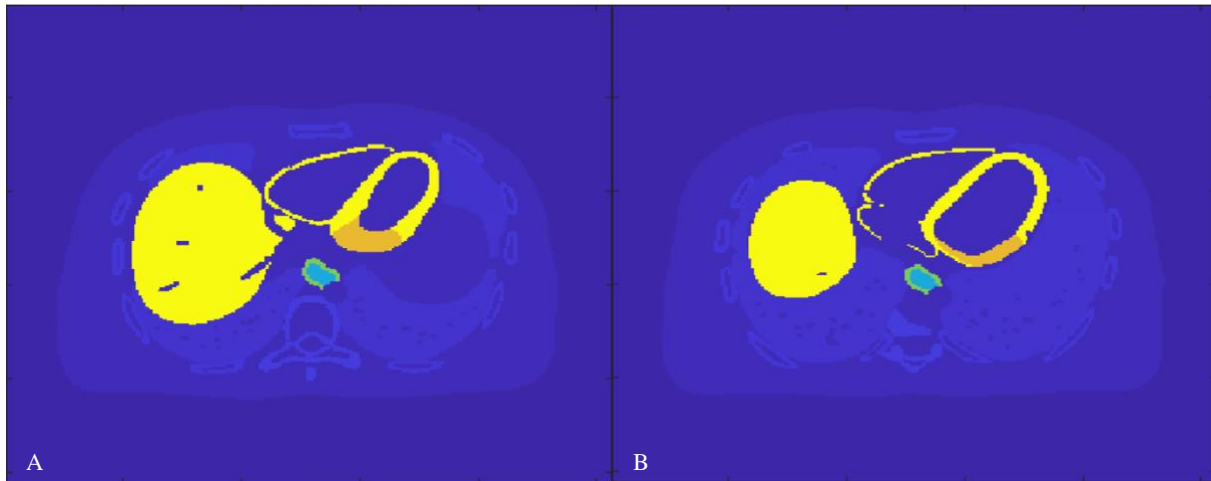


Figure 20. Transverse heart slices of a male Defect Present Phantom (DPP) at inferolateral wall of LV. (a) Slice 170; b) Slice 180.)

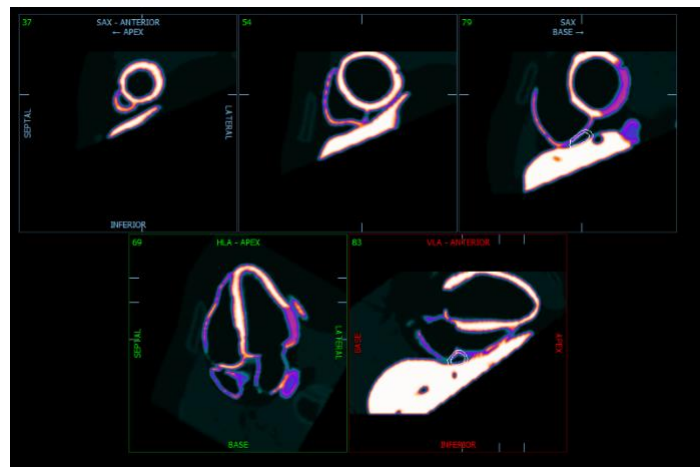


Figure 21. The lesion of Fig. 20 displayed in short-axis, horizontal long-axis and vertical long axis using CSImport.

Female Inferolateral Lesion

Similar correspondence is observed for the cohort of female DPPs. A female phantom of left ventricle volume 87.17ml is shown with a lesion of size 8.7ml at the inferolateral wall in Fig. 22. The inferolateral lesion can be seen in all three cardiac planes (from middle to base for short axis images).

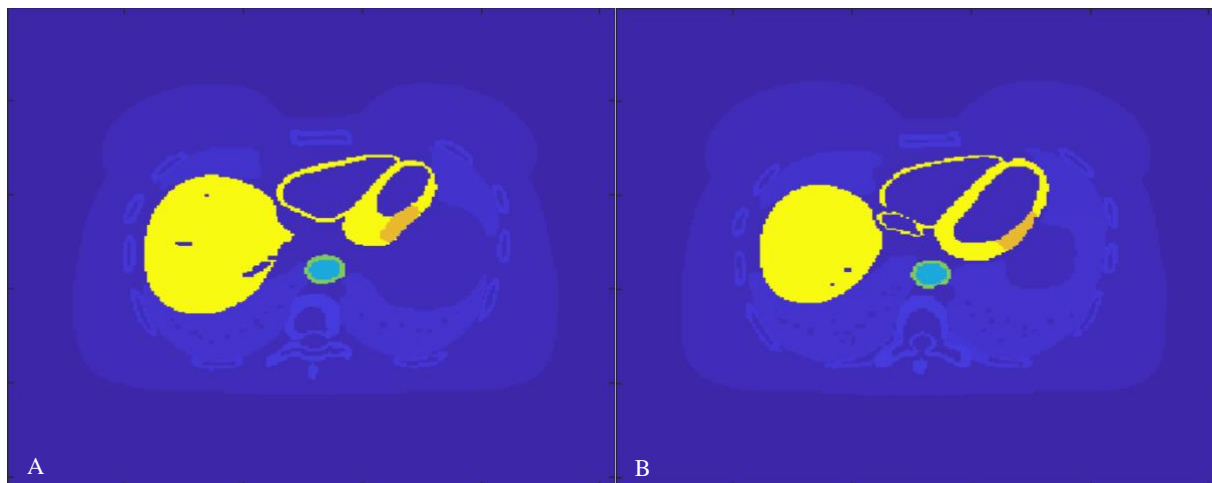


Figure 22. Transverse heart slices of a female Defect Present Phantom (DPP) at inferolateral wall of LV. (a) Slice 100; b) Slice 105.)

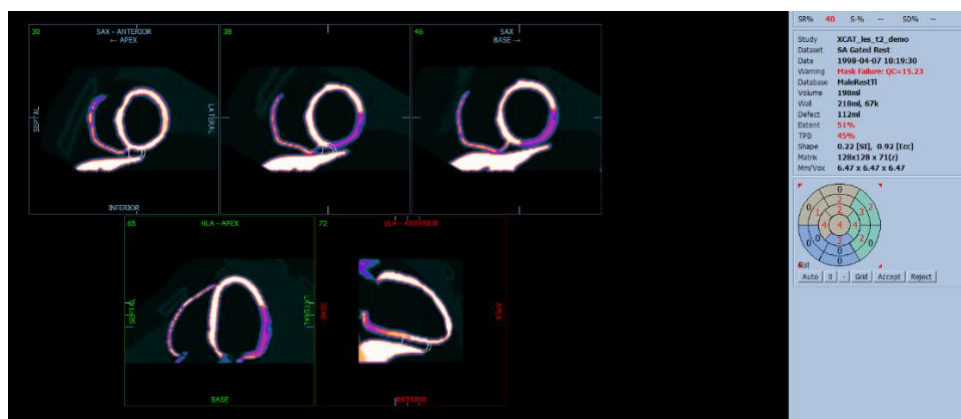


Figure 23. The lesion of Fig. 22 displayed in short-axis, horizontal long-axis and vertical long axis using CSImport.

For all perfusion defects defined in Table 2.2, we used the clinical software, CSImport, to verify their locations. Some images show the defect extends beyond the locations defined in the XCAT phantoms, e.g. the lesion at the apex. This commences the first part of this work to generate computer phantoms. These phantoms will then be simulated within a 20% energy

window using a LEHR collimator designed for ^{99m}Tc at an energy peak of 140 keV for 64 projection views on a 64×64 detectors in the next chapter.

CHAPTER 3

Monte-Carlo Simulation of Cardiac SPECT

Monte Carlo simulation is deemed as one of the most accurate methods in SPECT for calculating the photon events recorded by a conventional Anger camera or modern solid-state cameras. Combining the 4D XCAT phantom and SIMIND, the simulation can generate realistic imaging data similar to real patient data, yet with known ground truth for objective performance evaluation. In this work, we use SIMIND to simulate cardiac SPECT imaging with ^{99m}Tc -labeled Sestamibi. Activity and attenuation maps from the XCAT phantom are used as the inputs for SIMIND program.

3.1 Monte-Carlo Simulation Fundamentals

The core principle of Monte-Carlo methods (MCM) relies on unbiased samples through random selection from large data sets. With an average value of these unbiased samples, MCM estimates the actual value of the unknown parameter. This method becomes vital for extracting parameters in the photon counting process that characterizes Emission Tomography, as the time between each radioactive decay event does not follow deterministic laws. MCM performs simulations by first modeling a system as a series of probability density functions (PDF) which restrict the range of possibilities. These functions are then sampled and the parameters of interests, such as the number of ejected photons from an object incident on the detector, are calculated. For a photon source in an XCAT phantom, the probability of radioisotope decay is $[0, \infty)$, which can be modeled as an exponential distribution with the decay constant λ . The exponential distribution can be generated by a uniform distribution between the closed interval $[R, S]$. The uniform PDF for a selected range $R \leq u \leq S$ is given by:

$$p(u) = \frac{1}{S-R} \quad (8)$$

From this, we can obtain the cumulative probability function (CDF), which tells us the probability of a randomly sampled number that is no greater than u . CDF is represented as an integral of $p(u)$:

$$P(u) = \int_R^u \frac{1}{S-R} du = \frac{u-R}{S-R}, R \leq u \leq S. \quad (9)$$

Transferring a sample from the uniform distribution to a sample of another distribution can be conducted for any invertible CDF using an inversion method. For example, a random number u in the half-open interval $[0, 1)$ can be transferred to a random sample x following the exponential distribution as follows:

$$x = -\frac{\ln(1-u)}{\lambda}. \quad (10)$$

The PDF for the sampled x will follow the exponential distribution $f(x; \lambda) = \lambda e^{-\lambda x}$ for $x \geq 0$. Here, λ adjusts for the exponential decay inherent in the nuclear decay of the radioisotope.

When CDF inversion is computationally intensive, or analytically impossible, the acceptance-rejection method may be used to obtain random samples following the desired distribution more efficiently. To generate a random sample from PDF $f(x)$ (i.e. CDF $F(x)$), the acceptance-rejection method is:

- 1) Choose $G(x)$ with an invertible CDF (i.e. PDF $g(x)$) such that its multiplication with a constant c meets the condition: $c * G(x) \geq F(x)$ for all x .
- 2) Generate a random number w from $g(x)$.
- 3) Generate a random number v from the uniform distribution on the open interval $(0, 1)$.
- 4) If $c * v \leq \frac{f(w)}{g(w)}$, w is the random sample; otherwise, reject w and go back to step 2.

Once w has been sampled from $g(x)$, it is accepted or rejected in proportion to how much $c * g(x)$ overestimates $f(x)$ at w .

The photon generation from the nuclear decay, interaction with body materials (absorption and scatter) and detection by the camera all follow certain PDFs. Monte-Carlo simulation generates these random numbers using these PDFs and produces SPECT projection images.

3.2 Simulation of ^{99m}Tc -labeled Sestamibi SPECT imaging

The patient to be imaged is administered a dose of ^{99m}Tc -sestamibi with a half-life of ^{99m}Tc $t_{1/2} = 6.01$ hours. The tracer propagates through the electronegative transmembrane potential from the blood stream to the mitochondria matrix where they accumulate in the myocytes. Sestamibi is preferred clinically due to its high liver uptake and rapid blood clearance, with a heart uptake 1% of the injected dose after rest injection, and 1.4% dose after stress injection at 1 hour post intravenous injection.⁴ The ^{99m}Tc energy spectrum is shown in Fig. 24, where the photopeak energy is 140 keV.

Composed of a highly dense and absorbing septa, collimators designed with lead alloy selects for photons emitted by absorbing photons travelling in directions other than that specified by its hole-diameter. There are three types of collimator geometries: converging, parallel, and diverging. For example, a converging collimator can be used to image the brain so that the resolution can be improved without truncating the small organ.¹ Available in various hole shapes, collimators with hexagonal bores are widely used for maximum efficiency when coupled with a parallel geometry. Note that the distance dependent PSF related to the parallel-hole collimator occurs as discussed in Chapter 1. Four commercially available collimators are commonly used in medical clinics for SPECT imaging: low-energy high-resolution (LEHR), medium-energy high-resolution (MEHR), high-energy all-purpose (HEAP), low-energy all-purpose (LEAP). The low-energy (LE) collimators are suitable designs for detecting decays from radioisotopes in the range 69 keV- 159 keV. The ME and HE ranges correspond to planar imaging at a higher dose, thus each collimator designation is an indication of its trade-off between image resolution and sensitivity. For ^{99m}Tc scan, the 20% photon peak window (126-154 keV) are used to collect the photons for the efficiency and alleviate scatter effect.

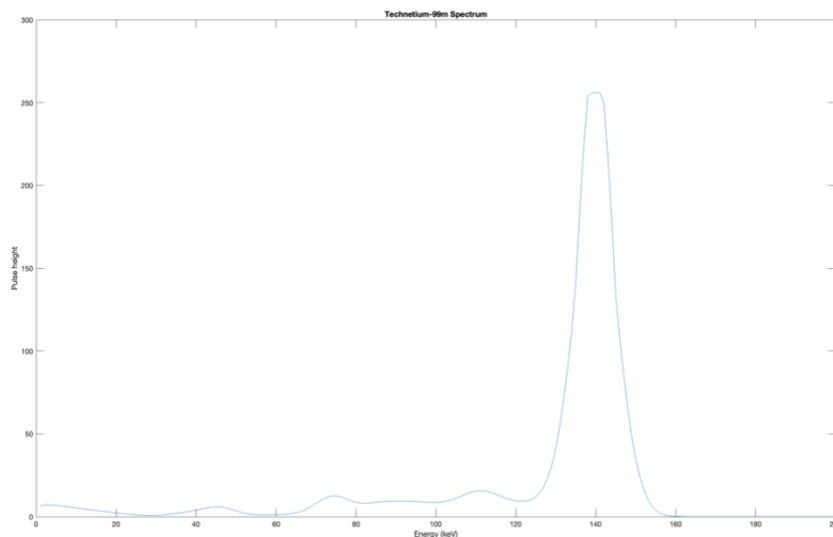


Figure 24. Energy spectrum of emitted photons of Tc-99m with the peak energy of 140 keV.

After the collimator, some of the gamma photons become incident on the scintillation crystal, producing an electronic signal used to determine the location of the photon-crystal event. The energy deposited on the crystal detector is then accepted if it is in the energy window around the primary emission peak of the radioisotope. If lower, this indicates the recorded photon experienced scatter somewhere in the data acquisition stage: in the patient upon radiotracer administration, at the collimator's aperture, or at the scintillator itself. Any of these interferences attenuates the photon energy and changes from its initial straight path, consequently reducing the image quality when accepted. The deposited energy is further converted into multiple visible light photons which propagates through the light guides to an array of photon multiplier tubes (PMTs) as shown in Fig. 25, where light photons are converted into electric current.¹ The light-output of the crystal detector is a spatially broad spectrum requiring several PMTs for conversion. The high-voltage PMTs are capable of outputting electric current proportional to the incident photon's energy.

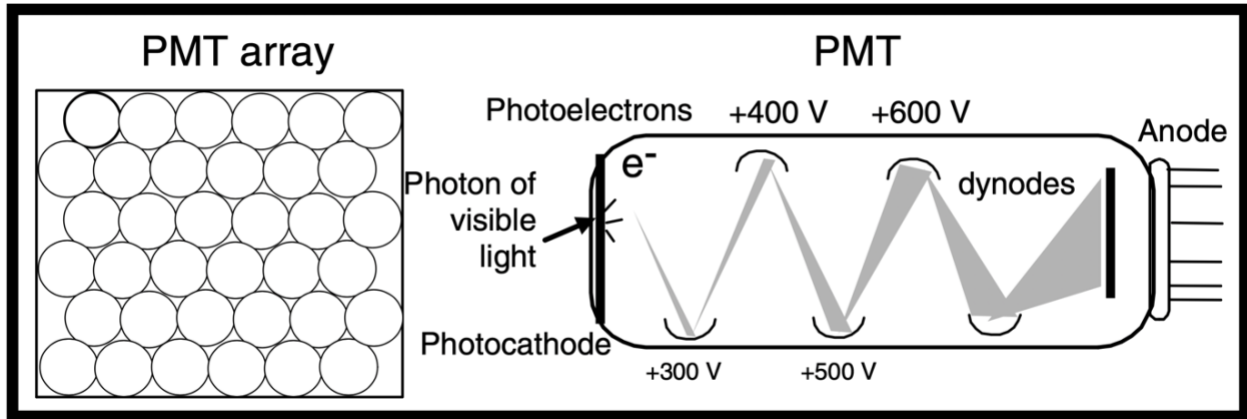


Figure 25. Schematics of a PMT array and its internal structure. A PMT consists of a photocathode, 6-10 dynodes and an anode. Voltage difference is maintained across the device during image acquisition¹.

3.2.1 Point-source results

The result, using an LEGP collimator and a 10% energy window (133 – 147 keV), for two point sources at a distance 2cm and 4cm away from the collimator is a scatter/primary of 77% and 88% respectively, and a scatter/total of 44% and 47% respectively. The energy spectrum This explains the low image quality observed for the point 4 cm from the collimator. The energy spectrum of all photons is shown in Fig. 27, which is quite different from Fig. 24 due to the scatter photons.

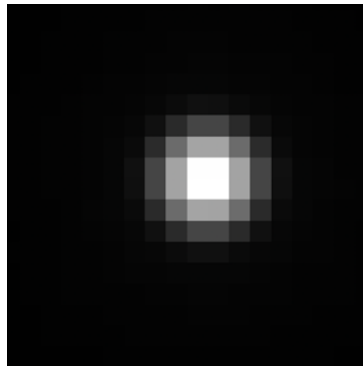


Figure 26. A point source 4cm away from the collimator at 10% energy window centered at 140 keV simulated with Tc-99m on SIMIND.

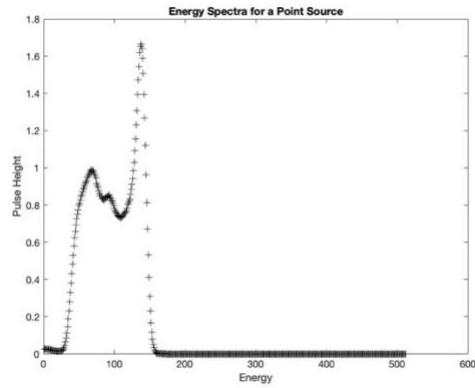


Figure 27. Tc-99m spectra for a point source.

3.2.2 Cold-spot phantom results

To test the SIMIND camera for non-uniform distribution expected from tracer interactions within the patient, small cylinders with no activity inside a high-activity cylinder was simulated as shown in Fig. 28. This is similar to the activity reduction of perfusion defect similar to the coldspot regions in Chapter 2.

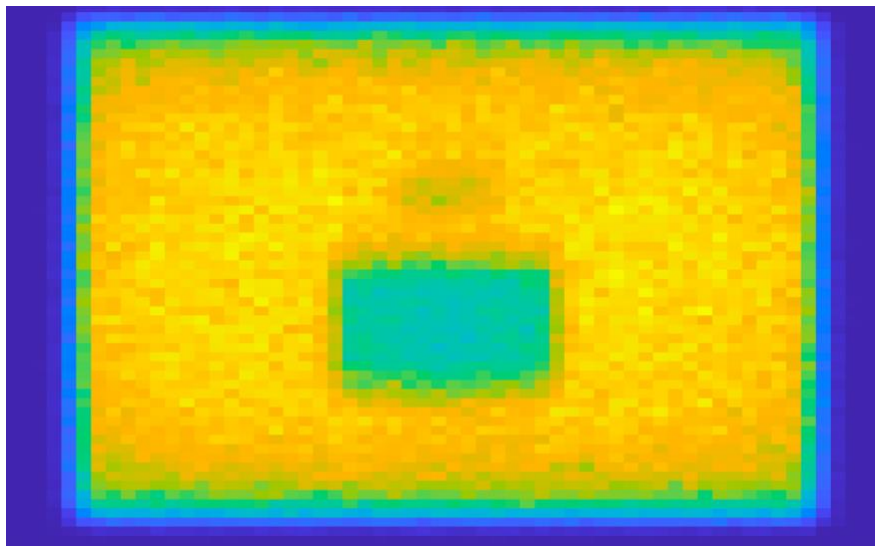


Figure 28. Projection image of a coldspot phantom.

3.2.3 XCAT phantom results

A male phantom with a total heart volume of 912.44 ml was simulated in SIMIND (using LEHR collimators) to generate the projection images that can be further processed test different reconstruction methods. The lead-antimony alloy collimator coupled with thallium-doped sodium crystal used for this simulation is expected to produce 4.667% photons for an

exposure to a peak energy of 140-keV at a 20% window. The pixel size for detector of the male phantom was set to .34 cm with a 64x64 array, while the XCAT phantom resolution is .15 cm. The pixel size and the array size are not large enough to cover the whole body as shown in Fig. 29, where part of liver was cut off. They could be increased to for future studies to obtain the complete projections from the activity maps. The camera sensitivity during the data acquisition process was recorded as 39.37 Cps/MBq. 64 projection views from the front of the phantom to the back covering 180° are shown in Fig. 30.

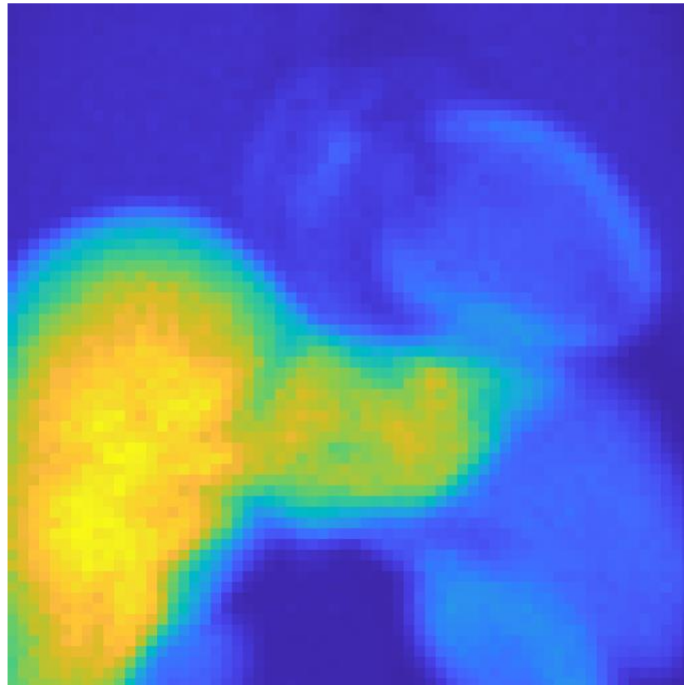


Figure 29. Projection image for a male phantom simulated in SIMIND, where a high uptake can be seen in the liver and the LV activity is due to the partial volume effect.

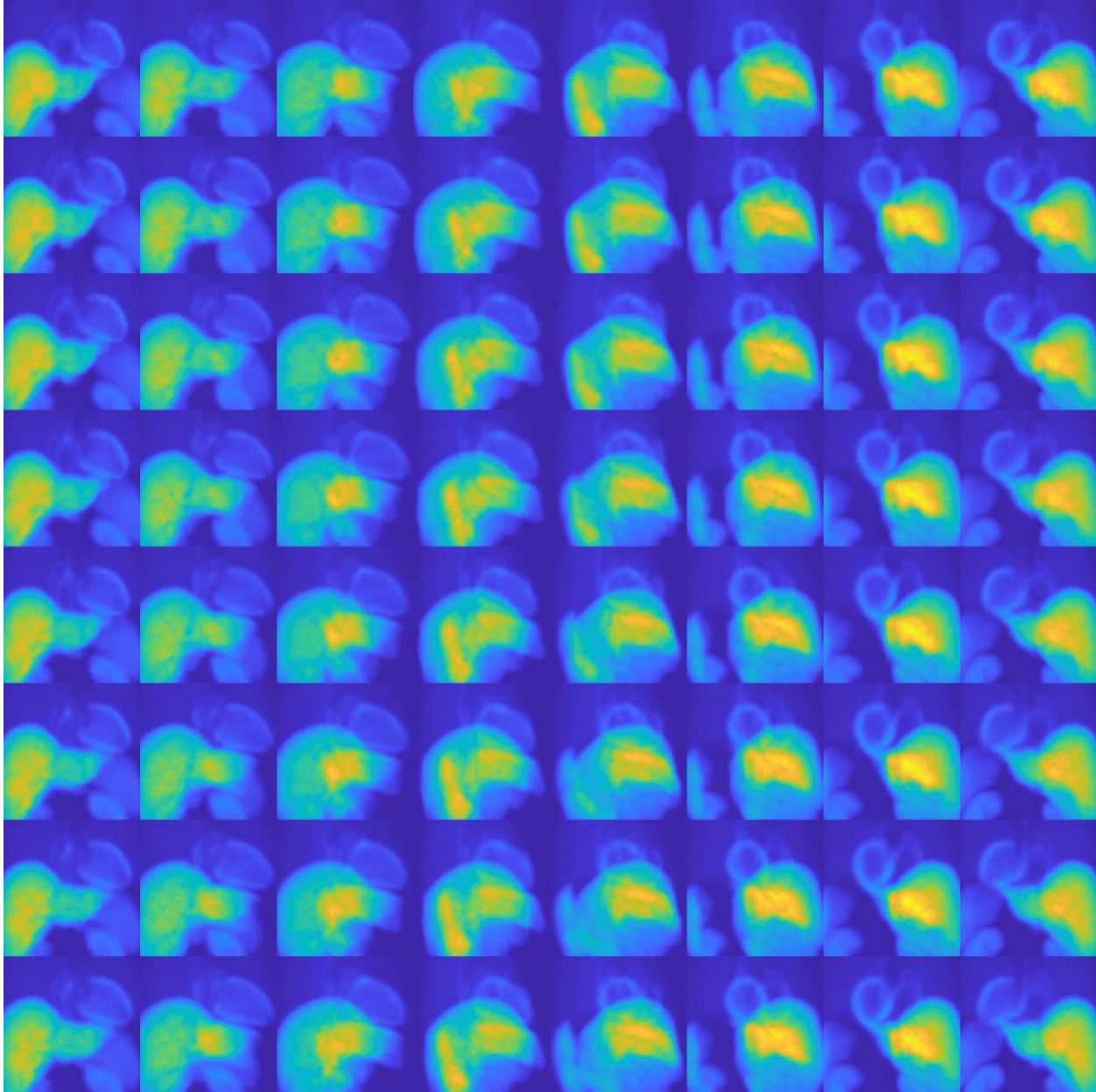


Figure 30. 64 projection images around 180° of a male phantom. The order is from top to bottom, then from left to right.

With the same detector parameter, a similar simulation was performed on a female phantom with a detector pixel size of .80 cm. Now the detector can cover the whole body width as shown in Fig. 31 and 32. The camera sensitivity for the female phantom was recorded as: 40.3622 Cps/MBq.

The generation of projection data for both male and female phantoms described in this chapter completes the second part of this work. The detail of settings in SIMIND can be found in Appendix.

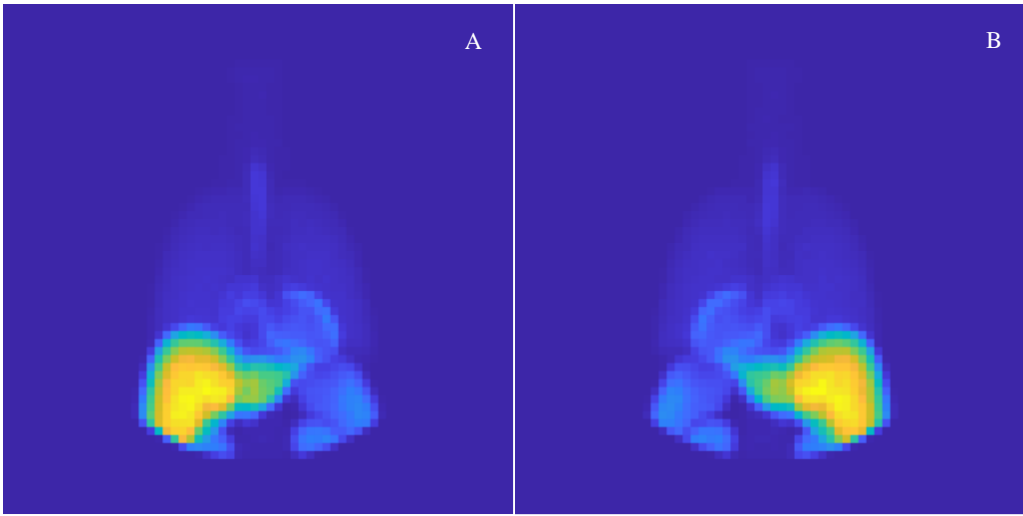


Figure 31. Projection images for a male phantom simulated in SIMIND (a: #1, front; b: #64, back)

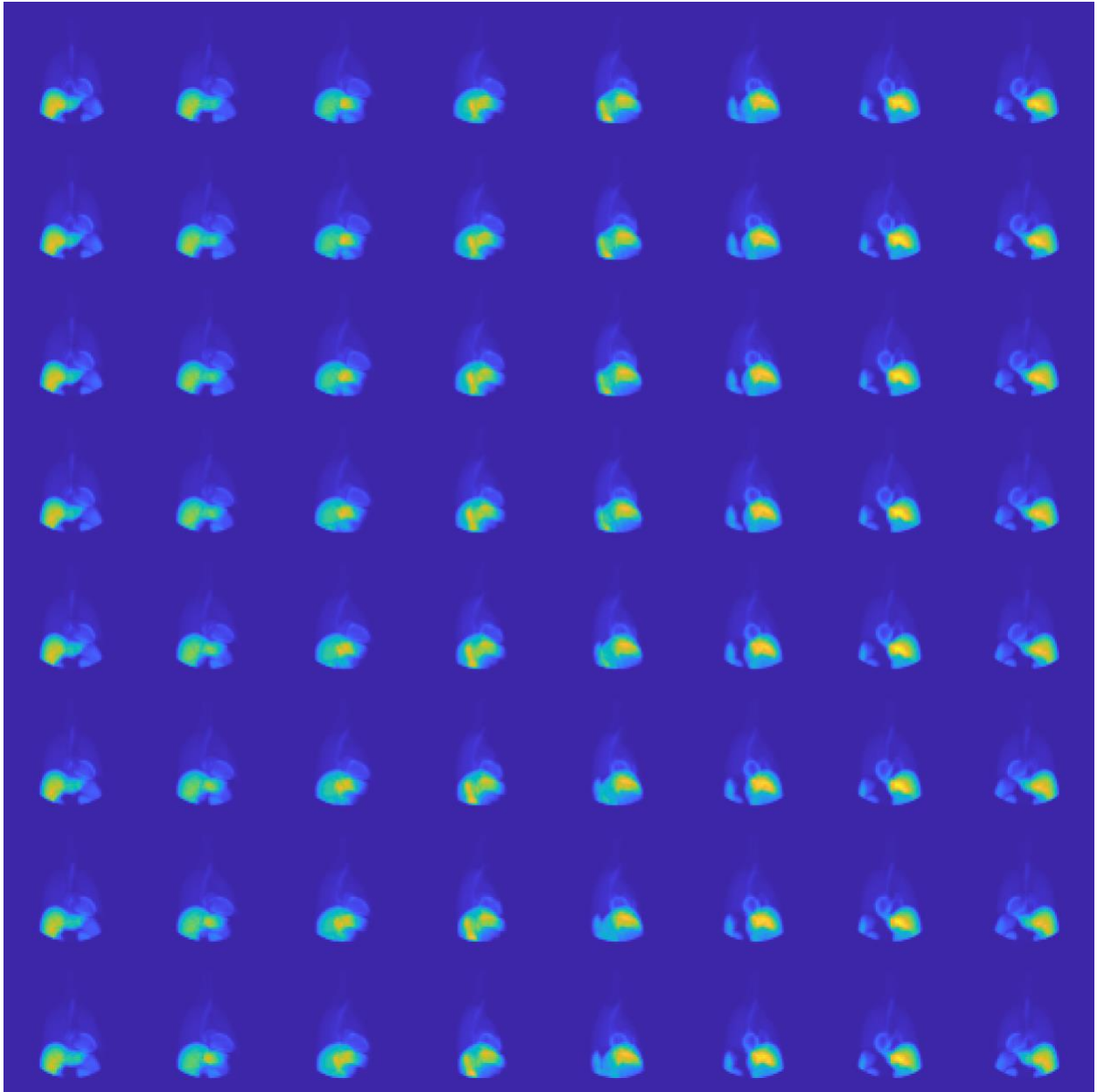


Figure 32. 64 projection images around 180° of a female phantom. The order is from top to bottom, then from left to right.

CHAPTER 4

Conclusion and Future Work

In this work, we first used the XCAT phantom program to generate different patient phantoms and different perfusion defects. The locations of these defects were verified using a clinical software. Then we simulated cardiac SPECT imaging of ^{99m}Tc -sestamibi using SIMIND Monte-Carlo simulation. The projection images of XCAT phantoms at different angles can be used to reconstruct 3D tracer distributions inside the phantom. This work lays a foundation for a mass simulation study for impact of motion-matched attenuation correction for dual-cardiac respiratory gated cardiac SPECT.

In the future, we first need to simulate the physiological motions, such as heart beating and patient breath. Then, the Poisson noise at the proper clinical count level needs to be added. The scatter photons will be collected in a scatter window for scatter correction. Then, the iterative reconstruction can be used to include mechanisms to correct for distance dependent PSF, noise, attenuation, scatter, and motion. In the simulation study, the attenuation maps are known. Thus, the upper bound of attenuation correction can be obtained. In real case, the attenuation maps can be obtained using 3 different strategies: (1) Importing from another modality, (2) Estimating attenuation map from the transmission data using the gamma camera employed for emission imaging, (3) Estimating the attenuation map only from the emission data. We will focus on attenuation maps from cone-beam CT (CBCT) and aim to minimize the artifacts for cardiac SPECT perfusion imaging.

Appendix 1- XCAT

The XCAT program contains more than 350 parameters, specifying body organs and regional heart motion defects. These base parameters were altered to generate the male and female phantom and their associated lesions. The defects are generated as described in Chapter 2. In XCAT parameter file, “ThetaWidth” and “XWidthIndex” specify the sizes of the lesions and “ThetaCenter” and “XCenterindex” specify the circumferential and axial position of the lesions. The part of the parameter file is shown below for definition of the lesion.

```
351 #-----Regional Heart Motion Defect-----
352 motion_defect_flag = 1 # (0 = do not include, 1 = include) regional motion abnormality in the LV as defined by heart lesion parameters see NOTE 9
353 #-----
354
355 #-----Heart lesion parameters-----SEE NOTE 9
356 ThetaCenter = 135 # theta center in deg. (between 0 and 360)
357 ThetaWidth = 140 # theta width in deg., total width (between 0 and 360 deg.)
358 XCenterIndex = .5 # x center (0.0=base, 1.0=apex, other fractions=distances in between)
359 XWidthIndex = 45 # x width, total in mm's. try less number next iteration
360 Wall_fract = 1 # wall_fract, fraction of the outer wall transgressed by the lesion
361 motion_scale = 1 # scales the motion of the defect region (1 = normal motion, < 1 = reduced motion), altered motion blends with normal
362
363 border_zone_long = 10 # longitudinal width (in terms of number of control points) of transition between abnormal and normal motion
364 border_zone_radial = 5 # radial width (in terms of number of control points) of transition between abnormal and normal motion
365 #-----
366
367 #-----Spherical lesion parameters-----SEE NOTE 10
368 x_location = 102 # x coordinate (pixels) to place lesion
369 y_location = 124 # y coordinate (pixels) to place lesion
370 z_location = 26 # z coordinate (pixels) to place lesion
371 lesn_diameter = 10.0 # Diameter of lesion (mm)
372 tumor_motion_flag = 0 # Sets tumor motion (0 = default motion based on lungs, 1 = motion defined by user curve below)
373 tumor_motion_filename = tumor_curve.dat # Name of user defined motion curve for tumor
374 #-----
375
376 #-----Heart plaque parameters-----SEE NOTE 11
377 p_center_v = 0.2 # plaque center along the length of the artery (between 0 and 1)
378 p_center_u = 0.5 # plaque center along the circumference of the artery (between 0 and 1)
379 p_height = 1.0 # plaque thickness in mm.
380 p_width = 2.0 # plaque width in mm.
381 p_length = 5.0 # plaque length in mm.
382 p_id = aorta # vessel ID to place the plaque in
383 *
```

A.1. Part of XCAT parameter file

Appendix 2- CSImport

The XCAT phantom files are in binary format. Upon rotating them into the proper orientation, they need to be transferred into the DICOM format before they can be imported in cardiac suite (CSImport) to generate the standard oblique slices. A typical import screenshot of CSImport is shown below.

The screenshot displays the CSImport software interface. The top section shows a list of studies with columns for Patient Name, ID/MRN, Other ID, Date of Birth, Sex, Status, Study Date, Modality, Assigned To, Accession #, and Referring. The bottom section shows a detailed view of a selected study with columns for Description, Dimensions, Date / Time, Isotope, T, S, G, P, DICOM Modality, and Camera.

Patient Name	ID/MRN	Other ID	Date of Birth	Sex	Status	Study Date	Modality	Assigned To	Accession #	Referring
Study, XCAT Femaleform	012345678		1994-02-14	M	XCAT test	1998-04-07 10:19:30	NM			
Study, Normal	111111		1934-02-14	F	Stress MIBI	1998-04-09 16:56:43	NM			
Study, Abnormal	012345678		1994-02-14	M	Rest Thallium	1998-04-07 10:19:30	NM			
SAdemo, XCAT	012345678		1994-02-14	M	XCAT_SAdemo	1998-04-07 10:19:30	NM			
Male_01_Lesson, XCAT	012345678		1994-02-14	M	XCAT_mes_demo	1998-04-07 10:19:30	NM			
Isdemo_02, XCAT	012345678		1994-02-14	M	XCAT_mes_demo	1998-04-07 10:19:30	NM			
Isdemo, XCAT	012345678		1994-02-14	M	XCAT_mes_demo	1998-04-07 10:19:30	NM			
Infesq, XCAT Female	012345678		1994-02-14	M	XCAT Female	1998-04-07 10:19:30	NM			
Infesq, XCAT Female	012345678		1994-02-14	M	XCAT Female	1998-04-07 10:19:30	NM			
Biv+L1, Patient	012345678		1994-02-14	M	Patient Biv+L1	1998-04-07 10:19:30	NM			
BP_TEST03	BP_TEST03		1996-03-07	U	BPM GATED	1996-03-07 16:01:12	NM			
BP_TEST01	BP_TEST01		N/A	F	REST GATED	1996-01-23 15:20:00	NM			
ArbEsp, XCAT Male	012345678		1994-02-14	M	XCAT Male	1998-04-07 10:19:30	NM			
ArbLat, XCAT Male	012345678		1994-02-14	M	XCAT Male	1998-04-07 10:19:30	NM			

Description	Dimensions	Date / Time	Isotope	T	S	G	P	DICOM Modality	Camera
ArbEsp, XCAT Male	XCAT Male	1998-04-07 10:19:30	MAI / 2044-02-14						UTA
SA Gated Rest + XCAT Male	161x139 x 1010	1998-04-07 10:19:30	Thallous chloride Tl-201	C				NM	
SA Gated Rest + XCAT Female	161x139 x 1010	1998-04-07 10:19:30	Thallous chloride Tl-201	C				NM	

A.2. DICOM file for male and female phantom in CSImport.

APPENDIX 3- SIMIND

The dimensions specified in the log file for each generic XCAT phantom are used to define half-length source and half-length Phantom in the Change program, which is used to define SIMIND simulation. Only emissions studies were performed, so simulation flag in the Change program returns false for Transmission studies. This can be accessed through index-3 on the main page of SIMIND. The parameters (>100) that can be defined in Change for SIMIND simulation are shown in A.3.

```
C:\simind\change.exe
C H A N G E: Scintillation camera parameters
1 - Photon energy.....keV: 140.0000
2 - Source: half-length Source.....cm: 24.0750
3 - Source: half-width Source.....cm: 0.0010
4 - Source: half-height Source.....cm: 0.0010
5 - Phantom: half-length Phantom.....cm: 24.0750
6 - Phantom: half-width Phantom.....cm: 0.0000
7 - Phantom: half-height Phantom.....cm: 0.0000
8 - Crystal: half-length/Radius.....cm: 20.0000
9 - Crystal: thickness.....cm: 0.3750
10 - Crystal: half-width.[0=Circular].....cm: 0.0000
11 - Backscattering material: Thickness.....cm: 0.3000
12 - Height to detector surface.....cm: 12.0000
13 - Thickness of cover.....cm: 0.2000
14 - Phantom type.....: -7.0000
15 - Source type.....: -7.0000
[22;07H[K Index number.....:
[2]H
C H A N G E: Scintillation camera parameters
16 - Shift source in x-direction.....cm: 0.0000
17 - Shift source in y-direction.....cm: 0.0000
18 - Shift source in z-direction.....cm: 0.0000
19 - Photon direction.....deg: 2.0000
20 - Upper window threshold.....keV: -20.0000
21 - Lower window threshold.....keV: -20.0000
22 - Energy resolution ...[140 keV].....%: 8.0000
23 - Intrinsic resolution [140 keV].....cm: 0.3600
24 - Emitted photons per decay.....: 0.8910
25 - Source activity.....MBq: 1.0000
26 - Number of photon histories * 1E6.....: 1000.0000
27 - keV/channel.....keV: 1.0000
28 - Pixel size in simulated image.....cm: 0.8000
29 - SPECT: No of projections.....: 64.0000
30 - SPECT: Rotation [0=-360,1=-180,2=360,3=180] : 1.0000
[22;07H[K Index number.....:
[2]H
C H A N G E: Non-homogeneous phantom and SPECT parameters
31 - Pixel size in density maps..... cm: 0.1500
32 - Orientation of the density map phantom.....: 0.0000
33 - Start image when reading density maps.....: 1.0000
34 - Number of CT-images.....: 321.0000
35 - Density limit defining the border..... g/cm3: 0.0000
36 - Shift density map relative origin (y-dir).cm: 0.0000
37 - Shift density map relative origin (z-dir).cm: 0.0000
38 - Step size for photon path simulation.....cm: 0.0500
39 - Shift density map relative origin.(x-dir).cm: 0.0000
```

```

C:\simind\change.exe
31 - Pixel size in density maps..... cm: 0.1500
32 - Orientation of the density map phantom..... 0.0000
33 - Start image when reading density maps..... 1.0000
34 - Number of CT-images..... 321.0000
35 - Density limit defining the border.... g/cm3: 0.0000
36 - Shift density map relative origin (y-dir).cm: 0.0000
37 - Shift density map relative origin (z-dir).cm: 0.0000
38 - Step size for photon path simulation.....cm: 0.0500
39 - Shift density map relative origin.(x-dir).cm: 0.0000
40 - Density threshold between soft & bone..g/cm3: 0.0000
41 - SPECT: Starting angle..... degree: 0.0000
42 - SPECT: Orbital rotation fraction.....: 1.0000
43 - Camera offset in x-direction.....cm: 0.0000
44 - Camera offset in y-direction.....cm: 0.0000
45 - Code definitions in generic Zubal phantom...: 1.0000
[22;07H[K Index number.....:
[22;07H[H
C H A N G E: Collimator parameters: GV-LEHR
46 - Hole Size X..... cm: 0.1500
47 - Hole Size Y..... cm: 0.1677
48 - Distance between holes in x-direction.....cm: 0.0200
49 - Distance between holes in y-direction.....cm: 0.1185
50 - Displacement center hole in x-direction...cm: 0.0050
51 - Displacement center hole in y-direction...cm: 0.1431
52 - Collimator thickness.....cm: 3.5000
53 - Collimator routine .....: 1.0000
54 - Hole shape:2=Cir,3=Hex,4=Rect.....: 3.0000
55 - Type: 0=PA,1=PI,2=CO,3=FB,4=DV,5=SH .....: 0.0000
56 - Distance from collimator to detector.....cm: 0.0000
57 - .....: 0.0000
58 - .....: 0.0000
59 - Random collimator movement (0=no).....: 1.0000
60 - .....: 0.0000
[22;07H[K Index number.....:
[22;07H[H
C H A N G E: Transmission simulation parameters
61 - Transmission photon energy.....keV: 0.0000
62 - Transmission photon polar angle..... degree: 0.0000
63 - Transmission photon azimuthal angle.. degree: 0.0000
64 - Source length.....cm: 0.0000
65 - Source width.....cm: 0.0000
66 - Shift transmission source in x-direction..cm: 0.0000
67 - Shift transmission source in y-direction..cm: 0.0000
68 - Shift transmission source in z-direction..cm: 0.0000
69 - .....: 0.0000
70 - Transmission option.....: 0.0000
[22;07H[K Index number.....:

```

```

C:\simind\change.exe
70 - Transmission option.....: 0.0000
[22;07H[K Index number.....:
[22;07H[H
C H A N G E: Imaging parameters and other settings
76 - Matrix size image I .....: 64.0000
77 - Matrix size image J .....: 64.0000
78 - Matrix size density map I .....: 256.0000
79 - Matrix size source map I .....: 256.0000
80 - Energy spectra channels .....: 512.0000
81 - Matrix size Density map J .....: 0.0000
82 - Matrix size source map J .....: 0.0000
83 - Cut-off energy to terminate photon history..: 0.0000
84 - Scoring routine .....: 0.0000
85 - CSV file content .....: 0.0000
[22;07H[K Index number.....:
[22;07H[H
C H A N G E: Solid state detector settings
91 - Voltage.....V: 0.0000
92 - Mobility life (electrons).....10-3 cm2/V: 0.0000
93 - Mobility life (holes) .....10-3 cm2/V: 0.0000
94 - Gap (fraction of detector size) .....: 0.0000
95 - Detector size .....cm: 0.0000
96 - Tau - exponential decay constant.....: 0.0000
97 - Hecht formula (e=0, e+h=1).....: 0.0000
98 - Energy resolution model .....: 0.0000
99 - Cloud mobility.....: 0.0000
100 - Detector Array Size I .....: 0.0000
101 - Detector Array Size J .....: 0.0000
[22;07H[K Index number.....:
[22;07H[H
C H A N G E: Main page for SIMIND version V6.2.1
1 - .....:
2 - Change some general data .....:
3 - Change simulation flags.....:
4 - Export to a SMC file.....: simind.smc
5 - Import from a SMC file.....:
6 - Clear all SMC data.....:
7 - Comment sentence.....:
8 - Transfer changes to other files:
9 - Phantom soft tissue.....file: h2o
10 - Phantom bone tissue.....file: bone
11 - Cover material.....file: al
12 - Crystal material.....file: nai
13 - Density map.....file: fp_br_ac1
14 - Source map.....file: fp_br_ac1
15 - Backscatter material.....file: lucite

```

A.3. Change program used to set Monte Carlo simulation parameters

REFERENCES

1. Wernick M, Aarsvold J. *Emmission Tomography*. Elsevier; 2004.
2. Xiaofeng N, Yongyi Y, Mingwu J, Miles NW, Michael AK. Effects of motion, attenuation, and scatter corrections on gated cardiac SPECT reconstruction. *Med Phys* 2011;38(12):6571–84.
3. Sakuma H, Ishida M. Advances in Myocardial Perfusion MR Imaging: Physiological Implications, the Importance of Quantitative Analysis, and Impact on Patient Care in Coronary Artery Disease. *J-STAGE* 2021;21(1):195–211.
4. Boschi A, Uccelli L, Marvelli L, Cittanti C, Giganti M, Martini P. Technetium-99m Radiopharmaceuticals for Ideal Myocardial Perfusion Imaging: Lost and Found Opportunities. *MDPI* [Internet] 2022;27(4). Available from: <https://www.mdpi.com/1420-3049/27/4/1188>
5. Segars WP, Bond J, Frush J, Hon S, Eckersley C, Williams HW, et al. Population of anatomically variable 4D XCAT adult phantoms for imaging research and optimization. *Med Phys* [Internet] 2013;20(4). Available from: <https://aapm.onlinelibrary.wiley.com/doi/10.1118/1.4794178>
6. Ljungberg M, Strand S-E. A Monte Carlo program for the simulation of scintillation camera characteristics. *Computer methods and programs in biomedicine*. 1989;29(4):257-272.
7. Schafer S, Jeffrey HS, Zhou K. Technology and applications in interventional imaging: 2D X-ray radiography/fluoroscopy and 3D cone-beam CT. [Internet]. In: *Handbook of Medical Image Computing and Computer Assisted Intervention*. 2020. page 625–71. Available from: <https://www.sciencedirect.com/science/article/pii/B9780128161760000314>
8. Saha K, Hoyt SC, Murray BM. Application of Chang's attenuation correction technique for single-photon emission computed tomography partial angle acquisition of Jaszczak phantom. *J Med Phys* 2016;41(1):29–33.
9. Rogers DF. *An Introduction to NURBS With Historical Perspective*. Morgan Kaufmann Publishers; 2001.
10. *Representation of Curves and Surfaces*. Robert McNeel & Associates [Internet] 2009; Available from: <https://web.mit.edu/hyperbook/Patrikalakis-Maekawa-Cho/node20.html>

11. Seagars WP. Realistic CT simulation using the 4D XCAT phantom. *Med Phys* 2008;35(8):3800–8.
12. Cerqueira MD, Weissman NJ, Dilsizian V. Standardized Myocardial Segmentation and Nomenclature for Tomographic Imaging of the Heart. *AHA* [Internet] 2002;105(4). Available from: <https://www.ahajournals.org/doi/10.1161/hc0402.102975>
13. Hutton BF, Allie R, Prvulovich E, Michopolou S. Pitfalls and artifacts using the D-SPECT dedicated cardiac camera. *J Nucl Cardiol* [Internet] 2016; Available from: <https://pubmed.ncbi.nlm.nih.gov/26403143/>